eman ta zabal zazu
Universidad del País Vasco
Euskal Herriko Unibertsitatea
BILBOKO INGENIARITZA ESKOLA
ESCUELA DE INGENIERÍA DE BILBAO

MASTER'S DEGREE IN

Space Science and Technology

MASTER'S THESIS

DIMENSIONLESS NUMERICAL ANALYSIS OF CRACKED MATERIALS BY MEANS OF INFRARED LOCK-IN THERMOGRAPHY

Student *Sagarduy Marcos, David*
Supervisor *Rodríguez Aseguinolaza, Javier*
Department *Applied physics*
Academic year 2021-2022

Bilbao, June 24th of 2022

Acknowledgments

I would like to thank to the Photothermal Technique Laboratory research group for all the help they have given me, with special mention to my supervisor Javier for the dedication and effort he has put into this work. The many hours we have spent trying to decipher the bash scripts and their entrails are now remembered as the titanic effort that has been made.

In these lines I cannot forget my parents. I would like to thank them for supporting me from the very beginning and giving me solutions when I didn't see them (even when I thought there were none!). Although only my name appears in the authorship of this work, it is as much mine as theirs.

Last but not least, I would like to thank my grandparents for the constant encouragement I have received from them over the years. Without it this would have been a much harder road.

Abstract

In this master's thesis a dimensionless numerical model of the lock-in infrared thermography experiment for the detection of open-surface cracks is developed. Starting with the constitutive equation and the boundary conditions associated with the laser and the cracks, their dimensions are removed by introducing length, time and temperature scales related to the physical problem. As a result, a set of dimensionless parameters is obtained, that allows to give a broader vision to the problem, while maintaining the mathematical simplicity of the dimensional model.

Once the dimensionless equations are obtained, they are implemented in a finite element method multiphysics software called OpenFoam. With this objective, in this work the full numerical calculation process has been developed: the pre-processing (or meshing), processing and post-processing stages.

After implementing the equations in the finite element method software a parametric analysis has been performed by means of different simulations in order to analyze the effect of each of the dimensionless parameter in the resulting amplitude thermogram.

Key words: Dimensionless equations, lock-in infrared thermography, finite element methods, OpenFoam, parametric analysis.

Resumen

En este trabajo fin de máster se desarrolla un modelo numérico adimensional del experimento de termografía infrarroja modulada para la detección de grietas superficiales. Partiendo de la ecuación constitutiva y de las condiciones de contorno asociadas al láser y a la grieta, se lleva a cabo el proceso de adimensionalización introduciendo escalas de longitud, tiempo y temperatura, asociadas al problema físico. Como resultado se obtiene un conjunto de parámetros adimensionales que permite dar una visión más amplia al problema, manteniendo a su vez la sencillez matemática del planteamiento dimensional.

Una vez adimensionalizadas, estas ecuaciones se implementan en un software multifísico de métodos de elementos finitos llamado OpenFoam. Para ello en este trabajo se contemplan las tres etapas de cálculo que se han seguido: el pre-procesado (o mallado), procesado y post-procesado.

Tras implementar las ecuaciones en el software del método de elementos finitos se realiza un análisis paramétrico mediante diferentes simulaciones con el fin de analizar el efecto de cada uno de los parámetros adimensionales en el termograma de amplitud resultante.

Palabras clave: Ecuaciones adimensionales, termografía infrarroja modulada, métodos de elementos finitos, OpenFoam, análisis paramétrico.

Laburpena

Master amaierako lan honetan, gainazalera irekitako pitzadurak detektatzeko termografia infragorri modulatuko esperimentuaren zenbakizko eredu adimentsional bat garatzen da. Eratze-ekuaziotik eta laserraren eta pitzadurak sartutako mugalde baldintzetatik abiatuta, adimentsionalizazio prozesua gauzatzen da, arazo fisikoari lotutako luzera, denbora eta tenperatura eskalak sartuz. Ondorioz, parametro adimentsionalen multzo bat lortzen da, arazoari ikuspegi zabalagoa emateko aukera ematen duena, eta, aldi berean, planeamendu dimentsionalaren sinpletasun matematikoari eusten diona.

Dimentsioak ezabatu ondoren, ekuazio horiek OpenFoam izeneko elementu finituen metodoen software multifisikoan inplementatzen dira. Horretarako, lan honetan jarraitu diren hiru kalkulu-etapak jasotzen dira: aurre-prozesatzea (edo saretzea), prozesatzea eta prozesatu ostekoa.

Elementu finituen metodoaren softwarean ekuazioak inplementatu ondoren, analisi parametriko bat egiten da hainbat simulazioren bidez, parametro adimentsional bakoitzak anplitude-termograman duen eragina aztertzeko.

Gako hitzak: Ekuazio adimentsionalak, termografia infragorria modulatua, elementu finituen metodoak, OpenFoam, analisi parametrikoa.

Contents

List of Figures

List of Tables

Acronyms

DG Discontinuous Galerkin.

DIC Diagonal Incomplete-Cholesky (symmetric).

DILU Diagonal Incomplete-LU (asymmetric).

FDIC Faster Diagonal Incomplete-Cholesky.

FEM Finite Element Methods.

FWHM Full Width at Half Maximum.

IR Infrared.

NDT Non-Destructive Testing.

OpenFoam Open Source Field Operation and Manipulation.

PCG Preconditioned Conjugate Gradient.

RMSE Root Mean Square Error.

1 Introduction

1.1 Context

The detection and characterization of both open-surface and hidden cracks is a challenge and a necessity to prevent failures in mechanical structures [1] since they play an important role in the strength of the industrial parts [2]. One of the sectors where the detection and characterization of cracks is of great importance is in the space and aeronautical sector. Since the different parts of the spacecraft are subjected to large thermal gradients and mechanical stresses, the appearance and growth of cracks is one of the problems to be taken into account. In fact, as an example, more than half of the material failures in the aeronautical sector are due to the crack growth [3].

In order to detect and characterize potential cracks, in addition to maintaining the operability of the material, non-destructive testing (NDT) measurement techniques are needed. Between these analysis methods, penetrating liquids, eddy currents, magnetic particles, X-ray tomography and infrared thermography can be found. Even though all of these techniques can be applied to crack detection, some of them may be quite expensive, such as the tomography, or may not be completely non-invasive, like the penetrating liquids. In contrast, thermographic methods are economically competitive and, above all, fully respect the integrity of the sample.

In this frame, infrared (IR) thermography has been proposed as a non-intrusive and safe method to detect quasi-superficial defects thanks to the pioneering work carried out by Kubiak [1]. In particular, this technique has been identified as a particularly appropriate one in order to detect cracks [4] as it is very sensitive to small defects in the studied surface.

Infrared thermography can be an active or passive technique. The difference between both approaches is that in the case of active IR thermography, the external heat source is not natural [5]. There are multiple options to create an external heat source, such as through the Joule effect or through optical excitation sources. The latter are the most developed and applied in the detection and characterization of cracks. In this methodology, a light source provides energy to the sample producing an increase in surface temperature and hence, the diffusion of heat in the material. Consequently, if there is any inner defect, it will be revealed by an abnormal temperature [6] in the images of the radiation detected by thermographic cameras, called thermograms.

Multiple lighting alternatives can be found. On the one hand, halogen or flash lamps can be chosen to illuminate the entire surface of the sample. This would produce a heat flux in-depth and would allow the detection of defects parallel to the surface, such as corrosion [6]. On the other hand, in-depth propagation and lateral heat flux, which would be disturbed by the presence of cracks, can be achieved by using a laser beam focused at the sample surface [6]. As a result, the thermogram would show a discontinuity in the temperature associated to the crack.

In terms of the nature of lighting, when using lasers, there are two main options:

1. Transient thermography: in this technique a sample is heated by a flash lamp and it is recorded by an infrared camera. If there are any defects, they could cause an abnormal heat flow and be revealed by the camera [7]. There are three main types of transient thermography:

    - Pulsed thermography: this technique consists in using a high power heat pulse in order to heat the surface of the sample and monitoring the cooling process [8].

- Continuous thermography: this lighting method uses a continuous heat source in order to heat the front surface of the solid and a thermal camera for detecting the time dependent temperature variations at the rear surface [9].
- Step thermography: in this method a long stepped pulse of low intensity is used and the surface temperature change is recorded during and after the application [10].

2. Lock-in thermography: this technique consists in illuminating the sample with a laser beam that varies harmonically in time while the surface temperature is recorded with a thermographic camera.

Among all the lighting techniques, lock-in thermography is the one which presents the lowest signal to noise ratio. This characteristic means that very small defects (in the order of microns) can successfully be measured, which has made this technique one of the most used in this field. However, laboratory measurements may not be enough to fully characterize the geometry of the crack. In consequence, mathematical modelling is needed in order to obtain all the quantitative information of the defects.

Taking into account that the geometry of the crack can be completely random, developing a mathematical model can be an extremely difficult task. An idealization that can be made in this sense is to suppose that cracks are straight, which leads to three main types of cracks: infinite, semi-infinite and finite cracks, introduced later in this work. However, an analytical solution can only be found in the case of an infinite vertical crack [11], which means that, in order to generalize the problem, finite element methods are needed.

Finite element methods (FEM) are general numerical techniques, where a continuous domain is discretized into a set of sub-domains called finite elements, for solving scientific problems described by partial differential equations [12]. The manner this equations are converted to a discrete problem is typically using Galerkin methods [12], which can be divided in three main types: continuous, discontinuous or mixed methods. When compared with other solving methods, one of the main advantages of FEM is that, as the domain is subdivided in multiple finite elements, it is a very flexible method in the sense that it allows to replicate complex geometries. In addition, they allow to introduce sophisticated physical phenomena such as thermal losses, thermal radiation or multiple cracks. Nowadays there are several software options in order to solve equations numerically with suitable capabilities for the physical phenomena addressed in this work, such as, FEniCS, GetFEM++ or OpenFoam.

In physics, in terms of solving the differential equations that govern a problem, there are two main approaches: dimensional and non-dimensional analysis. Even though both approaches solve exactly the same problem, there is a big difference between them. While the dimensional equations must be applied to specific cases, in terms of particular material properties or experimental conditions, the dimensionless model leads to a more general point of view, giving an insight into fundamental scales of the problem. Furthermore, the implementation of non-dimensional equations can lead to computational advantages, as they are arbitrarily scalables. This means that, for example, the spatial dimensions of the region can arbitrarily be resized in order to provide a better spatial resolution of the calculation. Considering these characteristics, in this work a dimensionless model will be developed describing the fundamentals of lock-in IR thermography.

This document is composed by six main sections. In the section 2 an experimental background is presented with the aim of providing basic concepts and a preliminary idea of the experiment that will later be numerically simulated.

In section 3 the equations to be implemented in the computational model are identified including

the laser and crack boundary conditions. After this equations have been nondimensionalized, and from the study of them, a set of dimensionless parameters is obtained that will be used to perform a parametric analysis.

In section 4 the computational part of this work is discussed, that is: the numerical schemes, the solution and algorithm control and the three stages that are carried out in the calculation: meshing, processing and post-processing. Moreover, in the meshing part, different mesh enhancement techniques are discussed in order to optimize the mesh resolution in the regions of interest.

The obtained catalog of curves is shown in section 5. Here, the validation process of the model has also been carried out. For this purpose, the developed non-dimensional model has been tested against the analytical solution and a different numerical model. The results obtained from these calculations are widely discussed in section 6. In this section, in addition to the validation, a complete parametric analysis of the dimensionless parameters is carried out.

Finally the conclusions and the future lines of this work are presented in the last section of this document.

1.2 Objectives

The main objectives of this work are the following:

1. Provide a physical-mathematical model to the lock-in IR thermography technique applied to cracked materials. This modeling consists in solving the heat equation numerically with the boundary conditions associated with the technique leading to thermal amplitude thermogram calculations.

2. Develop a numerical model in order to complement the lock-in IR thermography experiments keeping the mathematics as simple as possible and providing a quantitative description of the cracks.

3. Search for greater generality in the lock-in problem through a dimensionless model that provides more general information about the quantities that really affect to the thermal amplitude thermogram in the lock-in IR thermography experiment.

4. Use the dimensionless parameters resulting from the nondimensionalization process in order to carry out a detailed non-dimensional parametric analysis of the problem, as well as the identification of parameters associated to the system degeneracy.

5. Make use of the non-dimensional parameters in order to obtain a catalog of curves, where one of the parameters is varied while the rest remains fixed, that can be used as a guideline.

2 Experimental background

In recent years, great progress has been made in the detection of open-surface cracks by means of lock-in thermography. This experiments are carried out exciting the sample with a continuous laser beam of Gaussian profile whose intensity is modulated by means a mechanical chopper [11]. Once the intensity is modulated, the laser is focused by an optical lens system and directed perpendicular to the sample surface using mirrors [11]. In this configuration, the mirror must reflect the visible light and must also be transparent to the IR radiation in order to be able to record this radiation with the thermographic camera. A scheme of the experimental setup can be seen in figure 1.

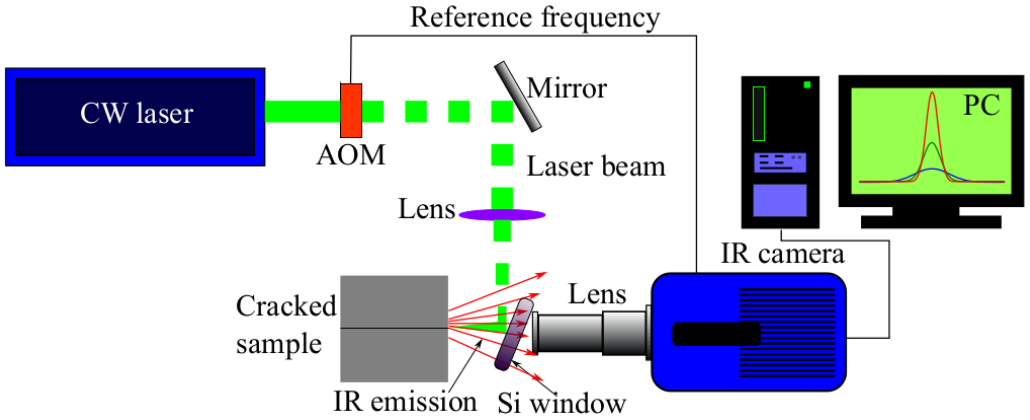

Figure 1: Typical laboratory lock-in IR thermography experimental setup.

In modulated thermography experiments, in order to obtain the thermogram, a set of experimental points are taken typically along a perpendicular line to the crack. Since in this experimental methodology a localized heating is observed, the thermal diffusion length μ [2] is introduced, i.e., the distance from the heat source where the heat is attenuated by a factor $1/e$.

Due to the harmonic nature of the heat source, the sample that is studied in lock-in IR thermography experiments,after a transitory stage, reaches a stationary state, as it is illustrated in figure 2. The temperature of the sample in the transitory stage can be expressed as follows [13]:

$$T(\vec{r},t) = T(\vec{r})\Big(1 + cos(2\pi ft)\Big) = T(\vec{r}) + \Re\Big(T(\vec{r})e^{-i2\pi ft}\Big) \tag{1}$$

where f is the frequency of the modulated laser beam. On the other hand, the temperature in the stationary state is [13]:

$$T(\vec{r},t) = T_{\text{room}} + T_{st}(\vec{r}) + \theta(\vec{r},t) \tag{2}$$

being T_{room} the room temperature, T_{st} the stationary rise in temperature of the sample from T_{room} and θ a temperature in harmonic regime:

$$\theta(\vec{r},t) = \Re\Big(T_{ac}e^{-i2\pi ft}\Big) \tag{3}$$

where θ is known as the thermal wave, which is the object of study in this experiment. Thus the result of the lock-in IR thermography experiment, in the stationary stage, is a set of thermal waves travelling

through the domain, characterized by their amplitudes and phases (see figure 3). In this project, the parametric analysis is going to be done with the amplitude.

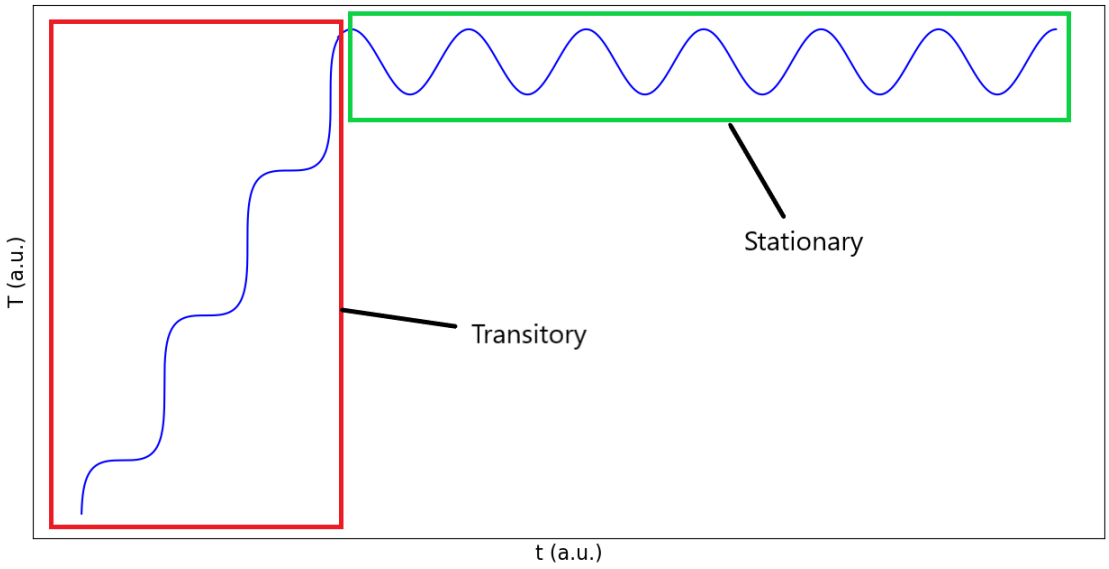

Figure 2: Scheme of the evolution of the surface temperature of the sample with harmonic laser heating.

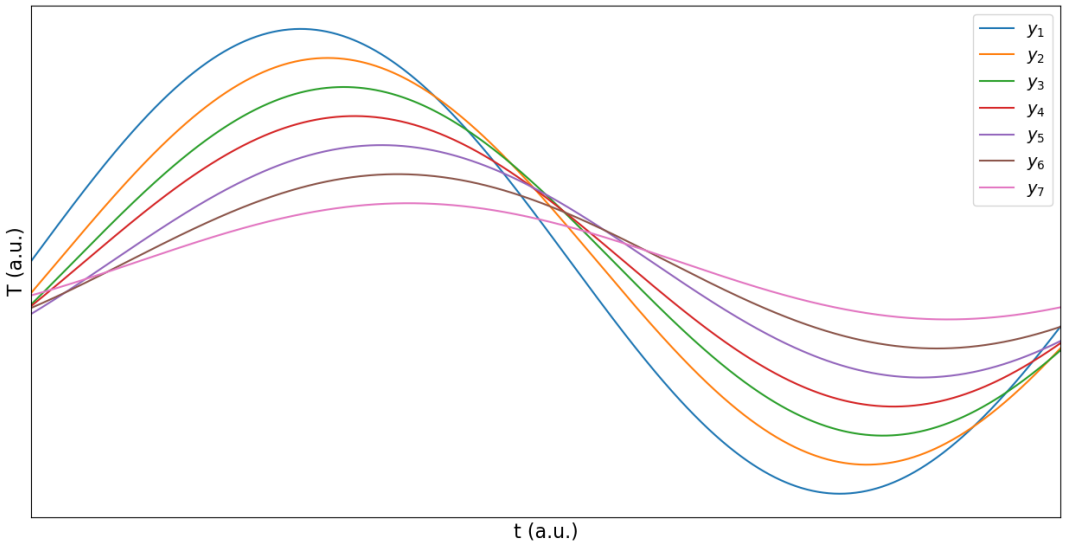

Figure 3: Scheme of the thermal waves in different points of the sample.

3 Theoretical model

3.1 Dimensionless equations

In order to develop a dimensionless computational numerical model of the crack detection problem by means of lock-in thermography, the first aspect that must be taken into account is the manner in which the dimensions of the set of equations that describe problem are removed. Due to the nature of the experiment, the constitutive equation is the heat equation:

$$\nabla^2 T = \frac{1}{\alpha}\frac{\partial T}{\partial t} \tag{4}$$

where α is the thermal diffusivity. Aiming to remove the dimensions of this equation the following variables are introduced:

$$\bar{x} = \frac{x}{L_x}, \quad \bar{y} = \frac{y}{L_y}, \quad \bar{z} = \frac{z}{L_z}, \quad \bar{T} = \frac{T}{T_0}, \quad \bar{t} = \frac{t}{t_c} \tag{5}$$

being L_x, L_y y L_z characteristic lengths of the problem in the three spatial directions, T_0 an arbitrary temperature (e.g., room temperature) and t_c a characteristic time value of the problem. Explicitly writing the heat equation and applying the chain rule:

$$\nabla^2 T = \frac{\partial^2(\bar{T}T_0)}{\partial \bar{x}^2}\frac{\partial^2 \bar{x}}{\partial x^2} + \frac{\partial^2(\bar{T}T_0)}{\partial \bar{y}^2}\frac{\partial^2 \bar{y}}{\partial y^2} + \frac{\partial^2(\bar{T}T_0)}{\partial \bar{z}^2}\frac{\partial^2 \bar{z}}{\partial z^2} = \frac{1}{\alpha}\frac{\partial(\bar{T}T_0)}{\partial \bar{t}}\frac{\partial \bar{t}}{\partial t} \tag{6}$$

Using the previously introduced parameters, this equation reduces to:

$$\frac{1}{L_x^2}\frac{\partial^2 \bar{T}}{\partial \bar{x}^2} + \frac{1}{L_y^2}\frac{\partial^2 \bar{T}}{\partial \bar{y}^2} + \frac{1}{L_z^2}\frac{\partial^2 \bar{T}}{\partial \bar{z}^2} = \frac{1}{t_c \alpha}\frac{\partial \bar{T}}{\partial \bar{t}} \tag{7}$$

A simplification that can be carried out at this point, and which is particularly convenient for computational calculations, is to choose the same length scale for all three spatial directions. Thus, imposing $L_x = L_y = L_z = L$ the dimensionless heat equation reduces to:

$$\bar{\nabla}^2 \bar{T} = \frac{\partial^2 \bar{T}}{\partial \bar{x}^2} + \frac{\partial^2 \bar{T}}{\partial \bar{y}^2} + \frac{\partial^2 \bar{T}}{\partial \bar{z}^2} = \frac{L^2}{t_c \alpha}\frac{\partial \bar{T}}{\partial \bar{t}} \tag{8}$$

where $\bar{\nabla}^2$ is the dimensionless Laplacian operator. In the process of removing dimensions of partial differential equations there are multiple criteria to choose the characteristic length and time scales. In particular, for the heat equation there are two main different criteria depending on the characteristics of the problem [14]:

1. $t_c = L^2/\alpha$, if heat diffusion occurs significantly throughout the domain. Here L is the length of the sample.

2. $t_c = 1/\omega$, if the change in temperature is significant only up to a certain limited distance, l. Here, ω is an angular frequency associated with the problem.

In lock-in IR thermography experiments, heat diffusion is a process that occurs up to distances from the heat source close to μ, where the heat is attenuated by a factor of $1/e$. Consequently, in this particular case, the second choice of scales is the most natural one, being $l = \mu$[1]. Choosing the characteristic length as μ the equation (8) reduces to:

$$\bar{\nabla}^2 \bar{T} = 2\frac{\partial \bar{T}}{\partial \bar{t}} \tag{9}$$

Here it has been used that $\omega = 2\pi f$ and the definition of thermal diffusion length: $\mu = \sqrt{\alpha/(\pi f)}$. For purely aesthetic reasons, the computational model has implemented the dimensionless heat equation with $t_c = 2/\omega$, so that the previous equation becomes:

$$\bar{\nabla}^2 \bar{T} = \frac{\partial \bar{T}}{\partial \bar{t}} \tag{10}$$

The second equation from which the dimensions must be eliminated is the boundary condition associated with the laser. In this case the laser, of power P, amplitude modulated at a frequency f and centered at (x_0, y_0, 0), is assumed to have a Gaussian profile and to be focused to a radius r_g (at $1/e^2$ of the maximum intensity) [6]. Therefore, the boundary condition in the stationary stage is:

$$-\kappa \frac{\partial T}{\partial z}\Big|_{z=0} = \frac{\eta P}{\pi r_g^2} e^{-2\left[\left(\frac{x-x_0}{r_g}\right)^2 + \left(\frac{y-y_0}{r_g}\right)^2\right]} \cos(2\pi f t) \tag{11}$$

being κ the thermal conductivity of the sample material and η the power fraction absorbed by the sample. In this work, the negative sign is introduced as a phase in the modulation term so it will no longer appear again. On the other hand, η is taken equal to one and a factor 2 is introduced because when the right hand side of the equation is integrated over x and y, without having that factor, the result is $P/2$. Taking this three details into account, this equation can be rewritten as follows:

$$\kappa \frac{\partial T}{\partial z}\Big|_{z=0} = \frac{2P}{\pi r_g^2} e^{-2\left[\left(\frac{x-x_0}{r_g}\right)^2 + \left(\frac{y-y_0}{r_g}\right)^2\right]} \cos(2\pi f t) \tag{12}$$

This boundary condition becomes dimensionless using the previously introduced variables:

$$(x, y, z) \to (\mu\bar{x}, \mu\bar{y}, \mu\bar{z}), \quad t \to \frac{2}{\omega}\bar{t}, \quad T \to \bar{T}T_0 \tag{13}$$

Therefore, applying the chain rule, the equation (12) becomes:

[1] In addition, this choice greatly simplifies the subsequent analysis of the problem based on the dimensionless parameters.

$$\frac{\partial \bar{T}}{\partial \bar{z}}\Big|_{\bar{z}=0} = \frac{2P\mu}{\pi r_g^2 T_0 \kappa} e^{-2\left[\left(\frac{\bar{x}-\bar{x}_0}{r_g/\mu}\right)^2+\left(\frac{\bar{y}-\bar{y}_0}{r_g/\mu}\right)^2\right]} \cos(2\bar{t}) \tag{14}$$

It must be noticed that the oscillation frequency of the laser heat source, in this dimensionless formulation, is no longer depending in any material or experimental parameters, being a constant value in any case. Once the dimensions of heat equation and laser boundary condition are removed, the two remaining equations are those associated with the crack. The constraints that must be satisfied are:

- The continuity of heat flow over the crack. This condition is written as follows:

$$[[\dot{Q}]] = 0 \tag{15}$$

  where the [[ ]] operator stands for the change on the flux over the crack [6]. Being equal to zero, removing the dimensions of this equations is straight forward:

$$[[\dot{\bar{Q}}]] = 0 \tag{16}$$

- A temperature discontinuity at crack position:

  The crack is modeled as a thermal contact resistance R_{th} [6], related to the width of the crack w through:

$$R_{th} = \frac{w}{\kappa_{air}} \tag{17}$$

  being κ_{air} the thermal conductivity of the air, which is assumed to fill the crack. Thus, the temperature discontinuity in the crack is given by:

$$\Delta T = \kappa R_{th} \nabla T = \kappa \frac{w}{\kappa_{air}} \nabla T \tag{18}$$

  Making use of the previously introduced dimensionless variables, this condition becomes:

$$T_0 \Delta \bar{T} = \kappa \frac{w}{\kappa_{air}} \frac{T_0}{\mu} \bar{\nabla} \bar{T} \tag{19}$$

  Here the dimensionless gradient operator $\bar{\nabla} \equiv \nabla/\mu$ has been introduced. Rearranging the terms, the dimensionless temperature jump condition due to the presence of a crack results in:

$$\Delta \bar{T} = \frac{\kappa}{\kappa_{air}} \frac{w}{\mu} \bar{\nabla} \bar{T} \tag{20}$$

Summarizing, introducing the thermal diffusion length μ as the length scale, $t_c = 2/\omega$ as the characteristic time scale and the temperature normalization factor T_0, the set of dimensional four equations that govern the physics of crack detection by lock-in IR thermography, becomes:

$$\begin{cases} \nabla^2 T = \frac{1}{\alpha}\frac{\partial T}{\partial t} \\ \left.\frac{\partial T}{\partial z}\right|_{z=0} = \frac{2P}{\kappa\pi r_g^2} e^{-2\left[\left(\frac{x-x_0}{r_g}\right)^2+\left(\frac{y-y_0}{r_g}\right)^2\right]}\cos(2\pi f t) \\ [[\dot{Q}]] = 0 \\ \Delta T = \kappa\frac{w}{\kappa_{air}}\nabla T \end{cases} \rightarrow \begin{cases} \bar{\nabla}^2 \bar{T} = \frac{\partial \bar{T}}{\partial \bar{t}} \\ \left.\frac{\partial \bar{T}}{\partial \bar{z}}\right|_{\bar{z}=0} = \frac{2P\mu}{\pi r_g^2 T_0 \kappa} e^{-2\left[\left(\frac{\bar{x}-\bar{x}_0}{r_g/\mu}\right)^2+\left(\frac{\bar{y}-\bar{y}_0}{r_g/\mu}\right)^2\right]}\cos(2\bar{t}) \\ [[\dot{\bar{Q}}]] = 0 \\ \Delta \bar{T} = \frac{\kappa}{\kappa_{air}}\frac{w}{\mu}\bar{\nabla}\bar{T} \end{cases}$$

It has to be mentioned that this entire work deals with the adiabatic problem, that is, it is assumed that there are no heat losses due to convection or radiation mechanisms. This decision is based on the nature of this two mechanisms. Radiation is proportional to T^4 which means that if the temperature is not high enough its effect is negligible. On the other hand, heat losses by convection are proportional to the difference between the room temperature and the sample temperature. However, IR thermography experiments are carried out a few kelvins above the room temperature so the difference is not large enough to be considered. Furthermore, this simplification is supported by the fact that, except in a few cases, the adiabatic model fits the experimental data relatively well.

3.2 Dimensionless parameters

Once the non-dimensional equations have been obtained, the terms that appear in the new equations can be rearranged to find characteristic independent dimensionless parameters which determine the nature of the problem. In particular, the combination of the terms that leads to these parameters can be found looking at the laser boundary condition (14) and the temperature jump condition at the crack (20). In both of them thermal conductivity κ appears, so, multiplying and dividing the boundary condition of the laser by the conductivity of the air, this equation becomes:

$$\left.\frac{\partial \bar{T}}{\partial \bar{z}}\right|_{\bar{z}=0} = \frac{2P\mu}{\pi r_g^2 T_0 \kappa_{air}} \frac{1}{\frac{\kappa}{\kappa_{air}}} e^{-2\left[\left(\frac{\bar{x}-\bar{x}_0}{r_g/\mu}\right)^2+\left(\frac{\bar{y}-\bar{y}_0}{r_g/\mu}\right)^2\right]}\cos(2\bar{t}) \tag{21}$$

Going further, in this equation the radius of the laser r_g appears both in the amplitude and in the exponential terms. So, it seems to be natural to multiply and divide the dimensionless modulation amplitude by the thermal diffusion length:

$$\left.\frac{\partial \bar{T}}{\partial \bar{z}}\right|_{\bar{z}=0} = \frac{2P}{\pi\mu T_0 \kappa_{air}} \frac{1}{\frac{\kappa}{\kappa_{air}}} \frac{1}{\left(\frac{r_g}{\mu}\right)^2} e^{-2\left[\left(\frac{\bar{x}-\bar{x}_0}{r_g/\mu}\right)^2+\left(\frac{\bar{y}-\bar{y}_0}{r_g/\mu}\right)^2\right]}\cos(2\bar{t}) \tag{22}$$

Defining the following dimensionless parameters:

$$\Pi_1 \equiv \frac{2P}{\pi\mu T_0 \kappa_{air}}, \quad \Pi_2 \equiv \left(\frac{r_g}{\mu}\right)^2, \quad \Pi_3 \equiv \frac{\kappa}{\kappa_{air}} \tag{23}$$

The laser boundary condition reduces to:

$$\frac{\partial \bar{T}}{\partial \bar{z}}\Big|_{\bar{z}=0} = \frac{\Pi_1}{\Pi_2 \Pi_3} e^{-\frac{2}{\Pi_2}\left[(\bar{x}-\bar{x}_0)^2+(\bar{y}-\bar{y}_0)^2\right]} \cos(2\bar{t}) \tag{24}$$

On the other hand, defining the dimensionless parameters associated to the crack geometry,

$$\Pi_w \equiv \frac{w}{\mu}, \quad \Pi_l \equiv \frac{l}{\mu}, \quad \Pi_d \equiv \frac{d}{\mu} \tag{25}$$

being l and d the length and depth of the crack, respectively, the temperature jump condition becomes:

$$\Delta \bar{T} = \Pi_3 \Pi_w \bar{\nabla} \bar{T} \quad \text{if} \quad \bar{x} \in \Big[-\frac{\Pi_l}{2}, \frac{\Pi_l}{2} \Big], \quad \bar{z} \in \Big[0, \Pi_d\Big] \tag{26}$$

Therefore, it is observed that, from the manipulation of two of the four equations and the definition of six dimensionless parameters, three associated with the geometry of the crack and three with the experimental conditions, a simplified non-dimensional formulation of the original equations is obtained. The equations to compute are summarized in the following box.

$$\boxed{\begin{cases} \bar{\nabla}^2 \bar{T} = \frac{\partial \bar{T}}{\partial \bar{t}} \\ \frac{\partial \bar{T}}{\partial \bar{z}}\Big|_{\bar{z}=0} = \frac{\Pi_1}{\Pi_2 \Pi_3} e^{-\frac{2}{\Pi_2}\left[(\bar{x}-\bar{x}_0)^2+(\bar{y}-\bar{y}_0)^2\right]} \cos(2\bar{t}) \\ [[\dot{\bar{Q}}]] = 0 \\ \Delta \bar{T} = \Pi_3 \Pi_w \bar{\nabla} \bar{T} \end{cases}} \tag{27}$$

In this work in addition to the parametric analysis associated to the mentioned six parameters, the position of the laser $(\bar{x}_0, \bar{y}_0)$ and the inclination of the crack θ will also be considered in the analysis in order to check their impact in the results.

IR thermography experiments in laboratories are typically carried out with lasers of power on the range of $0.1 - 10$ W, radius at $1/e^2$ of the maximum intensity is typically on the order of 10^{-4} m and are modulated at frequencies on the order of hertz. The cracks to be detected in these experiments are typically on the order of microns. As said before, in this experiments the interest is placed on the oscillation of the temperature so, the most natural choice of temperature scale T_0 is the maximum of the amplitude over the room temperature. Typically this values are on the order of few kelvins. Considering the mentioned variation ranges, table 1 shows typical values of the dimensionless parameters.

In this table it can be seen that the values of the first dimensionless parameter Π_1 can vary from 10^3 to 10^4 while values on the order of 10^{-4} or 10^{-1} are obtained for Π_2. A similar behaviour is found for Π_3, where values from 50 to almost 16000 are obtained. This leads to conclude that these three parameters are highly dependent on the material, which is a direct consequence of choosing the diffusion length as longitude characteristic scale. However, the same value of any dimensionless parameter can be obtained for different materials through the appropriate selection of the rest of experimental parameters.

	κ $(Wm^{-1}K^{-1})$ [15]	α (mm^2s^{-1}) [15]	Π_1	Π_2	Π_3
Cu	397.48	116.0	4685	0.0054	15899.2
AISI 304	14.64	3.68	28210	0.1963	600.0
Pb	34.309	23.3	10454	0.0270	1372.4
Lead Glass	1.13	0.74	58661	0.8490	45.2
Al	225.94	91.0	5289	0.0007	9037.6
Fe	71.965	20.4	11172	0.0307	2878.6

Table 1: Typical values of the dimensionless parameters for different materials. These values have been calculated with $P = 1$ W, $f = 5$ Hz, $r_g = 0.2$ mm, $T_0 = 2$ K.

4 Computational numerical simulations

There are two key aspects in computational numerical simulations: the mesh and the numerical method that is used to solve the equations. The manner the equations are translated from analytical formulation to computational formulation is an important aspect when using finite element methods because some numerical schemes may not work for some specific problems. In the following a brief description is these is given, even though it is not the scope of this work to go on further detail in this topic.

On the other hand, the mesh plays a key role in solving equations by numerical methods because it is, literally, where the equations are solved. This means that, in this case the simulated laboratory sample, has to be as similar as possible to a continuous medium but without having to spend much computational resources and time simulating the problem.

The simulations presented in this work have been carried out a workstation with Ubuntu MATE 20.04.4 with an Intel Xeon(R) Gold 5218 CPU @ 2.30 GHz $\times$ 64, 192 Gb memory and a graphic memory LLVM 12.0.0, 256b.

4.1 OpenFoam

Open Source Field Operation and Manipulation (OpenFoam) [16] is a C++ object oriented library, originally designed for computational fluid dynamics and structural analysis [17, 18]. However, after decades of evolution, it has become a software with multiphysics capacity oriented to a wide variety of physical phenomena, such as: combustion, electromagnetics, heat transfer and others. OpenFoam is used to create executables that fall in two categories: those that allow the manipulation of data, known as utilities, and solvers, which are designed to solve a specific problem in continuum mechanics [16].

Taking into account the nature of the problem to be solved in this work, among the variety of solvers that are implemented in OpenFoam, the solvers of the thermal family have been identified as the most suitable. Between all the options available, *solidFoam* has been selected as it has been designed for energy transport and thermodynamics on solids. In this solver not only complex boundary conditions, such as the ones of the laser or the crack, can be implemented but it could also benefit a future work in which this model is used to simulate flying spot experiments [19] because it allows to use dynamic meshes.

It is worth to mention that OpenFoam presents native parallel calculation capacity, which allows to distribute the nodes of the mesh between the available processes. Hence, this presents a double benefit. On the one hand, several simulations can be done simultaneously. On the other hand, faster calculations can be performed assigning each process a set of nodes.

4.2 Numerical schemes

As mentioned before, it is beyond the scope of this work to explain in detail the methods used to calculate the partial derivatives, gradients, etc. since the objective is to build the dimensionless model and these methods are equally valid for equations with and without dimensions. However, it should be mentioned that the schemes used have already been used to carry out simulations in similar physical phenomena with proven capabilities. The finite volume schemes that have been used in this work are

summarized in table 2.

Quantity	Scheme
Time partial derivatives	Crank Nicholson
Gradients	Gauss linear
Laplacian	Gauss linear corrected
Interpolations	Linear

Table 2: Finite volume schemes used.

4.3 Solution and algorithm control

In solution and algorithm control, the solver keyword specifies each linear-solver that is used for each discretised equation, that is, to the method of solving the set of linear equations [16]. On the other hand, the multiple options for preconditioning of matrices in the conjugate gradient solvers (DIC, FDIC, DILU,...) are controlled by the preconditioner keyword [16]. In this work the PCG solver and DIC preconditioner have been used as it has been seen that they suit properly to the characteristics of the problem.

In OpenFoam, the matrix solvers are based on reducing the error in the solution over an iterative process, that is, the residual is evaluated by substituting the current solution into the equation and taking the magnitude of the difference between the left and right hand sides [16]. In order to control if that difference is small enough, there are two variables that can be used:

1. Absolute tolerance: measures if the residual is small enough to consider the solution sufficiently accurate.
2. Relative tolerance: limits the relative improvement from initial to final solution.

Thus, the solution will be considered sufficiently accurate if the residual is lower than the absolute tolerance, or the ratio of current to initial residuals falls below the relative tolerance. In this work the absolute tolerance has been used as a measure of the accuracy of the simulation and it has been set to 1×10^{-7}.

Another aspect to be taken into account is the solution under-relaxation. This is a technique used for improving stability of a computation that can be applied in physical simulations where variables vary that fast that can lead to numerical divergences. Since the nature of the experiment that is being simulated does not imply this kind of problems, the relaxation factor in this work is left as default, that is, equal to 1. The solution and algorithm control configuration used in the simulations is shown in table 3.

Solver	Preconditioner	Absolute tolerance	Relative tolerance	Relaxation factor
PCG	DIC	1×10^{-7}	0	1

Table 3: Solution and algorithm control keywords used.

4.4 The mesh

As said before, the mesh plays a key role in computational numerical simulations. There are two main strategies to simulate cracks in materials. The first one is to model the problem as a two domain material: the bulk and the air filling the crack. This strategy implies that, close and inside the crack, an extremely fine mesh has to be done which dramatically increases memory resources and calculation time due to the difference in spatial scale between the crack and the bulk [20, 21]. The second option is to model the crack as a contact thermal resistance surface. In this approach, there is no crack volume to mesh, because the latter is modeled as a 2D plane [2, 6], notably reducing the computational resources required.

In OpenFoam there are two main options to model a crack. The first one consists in using the function already implemented in OpenFoam, which allows to create the sample as an entire block and then define the geometry of the crack. This method allows the user to simulate as many cracks as wanted without adding complexity to the mesh. However, this strategy has a big drawback: it implies that the geometry of the crack will be rounded to the values to the nearest node of the mesh, meaning that the crack will no longer be as wide, long or deep as it had been modeled.

The second option is to reproduce the crack as a contact surface between hexahedral blocks, which implies that the sample has to be divided into multiple domains that later have to be joined. In other words, the sample has to be constructed 'block by block'. Since the number of blocks to create depends entirely on the type of crack (infinite, semi-infinite or finite), the main disadvantage of following this path is that the complexity of the code increases. On the other hand, following this methodology ensures, by construction, that the crack will have the desired dimensions. As a consequence, in this work, this has been the followed meshing strategy.

Another key aspect to be taken into account is the geometry of the mesh. Among all the options, the most used meshes are tetrahedral and hexahedral meshes. These two types of meshes and the individual elements can be seen in figures 4 and 5.

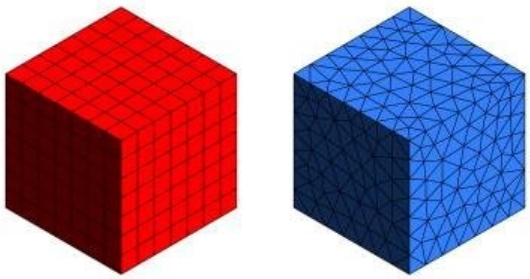

Figure 4: (left) Hexahedral and (right) tetrahedral meshes.

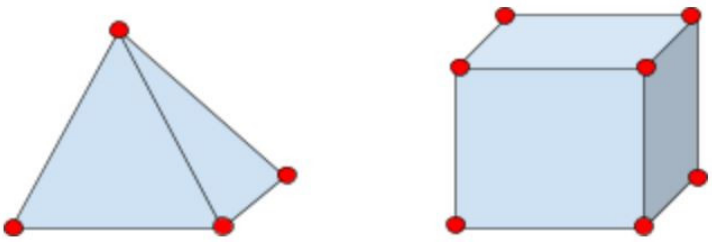

Figure 5: (left) Tetrahedral and (right) hexahedral mesh elements.

Tetrahedral meshes are made up of elements with 4 vertices. These can be rearranged so that a

higher resolution is acquired in one part of the mesh than in another simply modifying the density of elements in that region. This can be done due to the versatility offered by the geometry of the elements. On the other hand, hexahedral meshes are made up of elements with 8 vertices, which means that, without further refinement, there is no longer the possibility to modify the density of elements in a concrete region to obtain more resolution. However, in regular grids such as the obtained with hexahedral elements, there are three different possibilities to achieve an increase in resolution: increase the number of elements in the entire mesh, introduce a local gradient or a refinement. This last two options are explained in detail in section 4.5.

Despite being computationally more expensive meshes, hexahedral ones tend to be more accurate than the tetrahedral ones for the same number of nodes [22] because of the number of vertices of each individual element. While tetrahedral elements only have 4 vertices, hexahedral elements have 8. This implies that when interpolations between nodes are performed, in a hexahedral mesh the interpolation will be done with more information because there are more nodes nearby and, consequently, the solution will be more accurate.

In this work the meshes have been made with the native OpenFoam mesher so the type of mesh that has been used is the hexahedral one. Mathematically the meshed domain is defined as follows:

$$\left\{(\bar{x},\bar{y},\bar{z}) \in \mathbb{R}^3 | \bar{x} \in [\bar{x}_{min},\bar{x}_{max}], \bar{y} \in [\bar{y}_{min},\bar{y}_{max}], \bar{z} \in [0,\bar{z}_{max}]\right\} \tag{28}$$

4.4.1 Infinite cracks

A crack is said to be infinite if its length and depth are much larger than the thermal diffusion length of the material. In this case an analytical solution is available only for cracks perpendicular to the surface [1], whereas FEM is needed for the rest of tilting angles. Due to the fact that $l, d >> \mu$, the modeling of this case can be done supposing that the length and depth of the crack is equal to those of the sample (ensuring that it is big enough), as it is shown in figure 6. This means that, to model the sample, two blocks are needed. This blocks can be distinguished in figure 7. The spatial limits of the infinite crack are:

$$\begin{cases} \bar{x}_c \in [\bar{x}_{min},\bar{x}_{max}] \\ \bar{y}_c \in [0,\bar{z}_{max}/tg(\theta)] \\ \bar{z}_c \in [0,\bar{z}_{max}] \end{cases}$$

where θ is the angle of inclination with respect to the surface illuminated by the laser. The relation between the maximum limit in $\bar{y}$ and $\bar{z}_{max}$ is obtained by geometry since, as can be seen in the crack diagram 6:

$$tg(\theta) = \frac{\bar{z}_{max}}{\bar{y}_{c,max}} \tag{29}$$

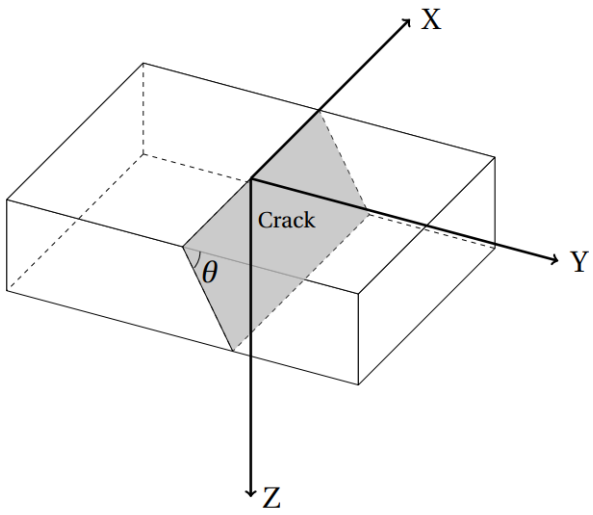

Figure 6: Scheme of an infinite crack

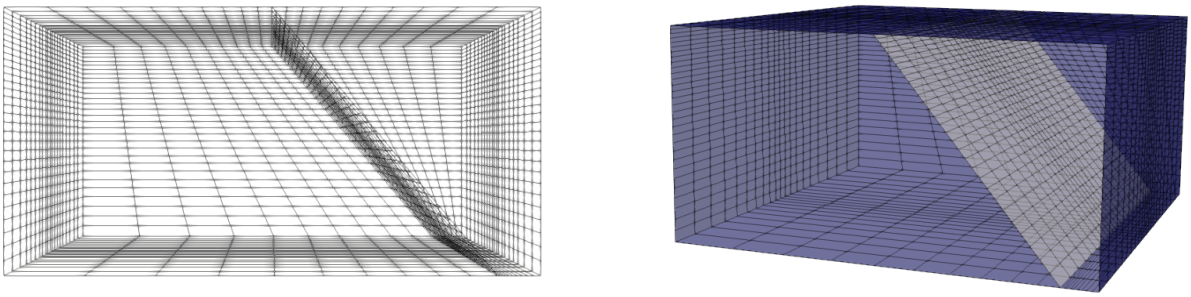

(a) (b)

Figure 7: (a) The two blocks that make up the infinite crack and (b) the final result.

4.4.2 Semi-infinite cracks

A semi-infinite crack is a slightly more general case than the infinite crack. The name semi-infinite alludes to the fact that it is larger than the thermal diffusion length in one of the directions but it is comparable to μ in the other one. In this work it will be assumed that the length of the crack in the $\bar{x}$ direction is much longer than the thermal diffusion length but its depth is at least comparable to it. In this case, the regions $\bar{z} < \Pi_d$ and $\bar{z} > \Pi_d$ also have to be distinguished provided that the interface between blocks is conformal. Taking this into account four are needed.

In terms of the coordinates of the crack, the unique change with respect to the previous case is that the maximum value of $\bar{z}_c$ changes from $\bar{z}_{max}$ to Π_d. Summarizing, the semi-infinite crack coordinates are:

$$\begin{cases} \bar{x}_c \in [\bar{x}_{min}, \bar{x}_{max}] \\ \bar{y}_c \in [0, \Pi_d / tg(\theta)] \\ \bar{z}_c \in [0, \Pi_d] \end{cases}$$

being θ the angle of inclination. The four blocks and the final mesh can be seen in the figure 8.

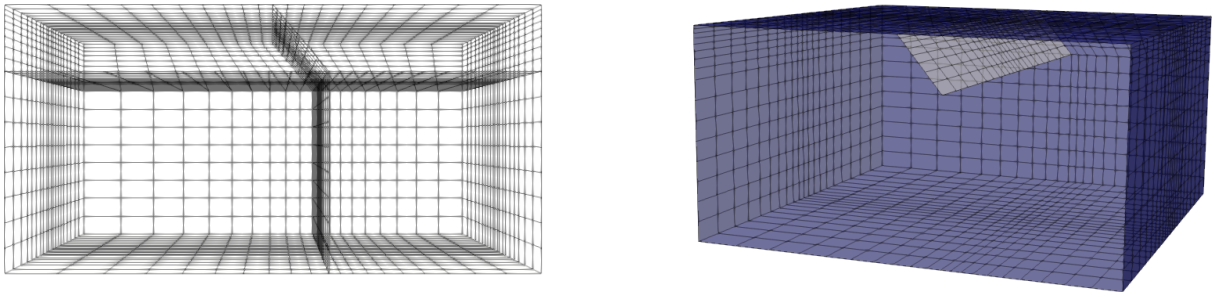

(a) (b)

Figure 8: (a) The four blocks that make up the semi-infinite crack and (b) the final result after joining them.

4.4.3 Finite cracks

The finite crack is the most general case among the three considered. In this case the crack is not long and/or deep enough to consider those dimensions much greater than μ. In addition to distinguish the regions $\bar{z} < \Pi_d$ and $\bar{z} > \Pi_d$, just as it is done in the semi-infinite crack case, the regions $\bar{x} < -\Pi_l/2$, $\bar{x} \in [-\Pi_l/2, \Pi_l/2]$ and $\bar{x} > \Pi_l/2$ have also to be distinguished, which means that the number of blocks rises from 4 to 12. This blocks are shown in figure 9 and the final mesh in figure 10. In this case the coordinates are:

$$\begin{cases} \bar{x}_c \in [-\Pi_l/2, \Pi_l/2] \\ \bar{y}_c \in [0, \Pi_d/tg(\theta)] \\ \bar{z}_c \in [0, \Pi_d] \end{cases}$$

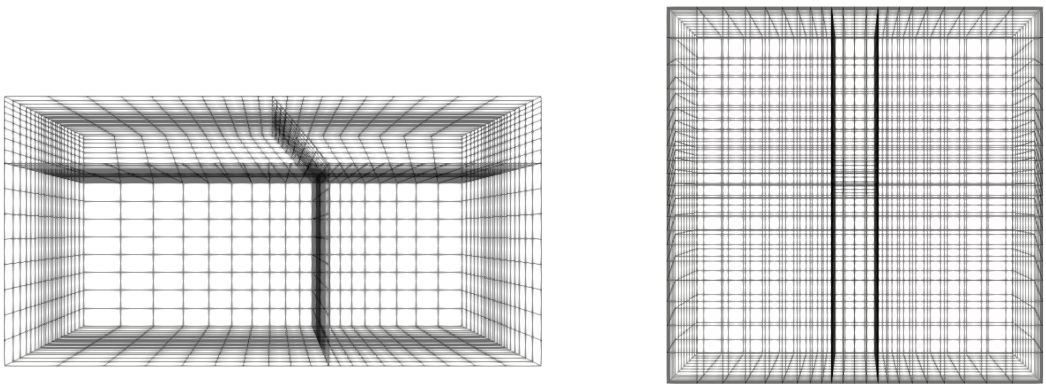

(a) (b)

Figure 9: (a) Lateral view in the $+\bar{x}$ direction showing the corresponding four blocks and (b) zenital view in the $+\bar{z}$ direction showing the corresponding three blocks.

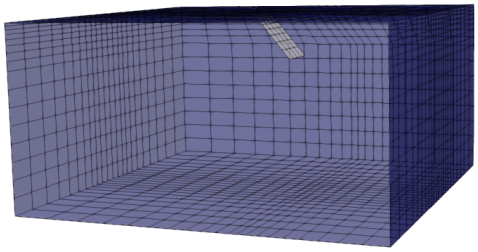

Figure 10: Final result after joining the corresponding twelve blocks.

4.5 Mesh resolution control

With the objective of improving the spatial resolution of the mesh in the regions where the studied variables change more abruptly, i.e., where more physical information can be found, in this work two complementary methods have been implemented. It is worth to mention that, even though the dimensionless model is being implemented, the methodologies presented in this section are also valid for the case with dimensions.

4.5.1 Mesh element distribution gradient

The native mesher of OpenFoam allows not only to determine the number of lines in each spatial direction but also to modify the spacing between edges, that is, to establish a gradient of nodes. Since no new nodes are spawned, but simply redistributed, this method to increase the mesh resolution in a specific region does not increase the computational resources that are needed. Hence, it seems to be natural to establish a gradient in all three spatial directions in order to increase the resolution in the region close to the crack.

Since in the $\bar{y}$ and $\bar{z}$ directions the blocks are joined in pairs, establishing a gradient that ensures the continuity of the distribution of nodes is a trivial task, but in the $\bar{x}$ direction this depends on the casuistry that is being contemplated.

In the infinite and semi-infinite cracks implementing a spatial gradient in the $\bar{x}$ direction does not add any complexity because only two blocks have to be joined. In the finite crack, by contrast, as the regions previously mentioned have been distinguished, three blocks have to be joined on each side of the crack in that direction. This means that the way to match the distance between edges is not so obvious. The scheme of the problem that is going to be solved is shown in figure 11.

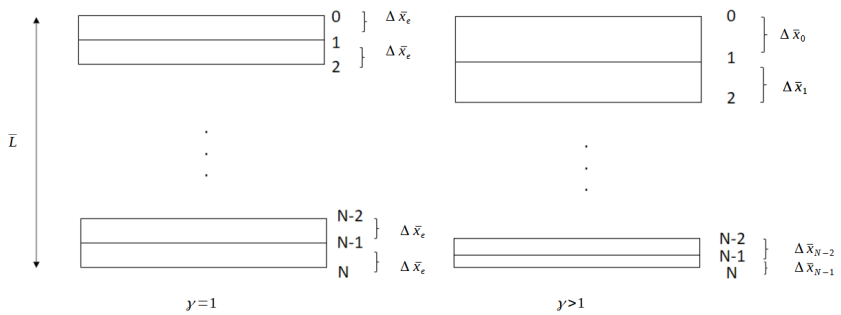

Figure 11: Diagram of the spacing between mesh edges. Left: regular distribution. Right: downward spatial grading.

Let $\Delta\bar{x}_e$ be the distance between the nodes when they are evenly spaced:

$$\Delta\bar{x}_e = \frac{\bar{L}}{N} \tag{30}$$

where $\bar{L} = \bar{x}_{max} + |\bar{x}_{min}|$ and N is the number of edges. Let $\Delta\bar{x}_0$ be the distance between the first two nodes when a gradient ($\gamma \neq 1$) is introduced. Then the relationship between the distance from edge $i-1$ to edge i and $\Delta\bar{x}_0$ can be:

$$\Delta\bar{x}_i = \Delta\bar{x}_0 - \Delta\bar{x}_0 f \tag{31}$$

where f is a function that must satisfy the following conditions:

1. Its value must increase while i increases.
2. $f(i=0) = 0$.
3. If $i = N-1$ then: $\Delta\bar{x}_{N-1} = \Delta\bar{x}_0/\gamma$.

The simplest function that satisfies those three conditions is:

$$f = \frac{i}{N-1}\Big(1 - \frac{1}{\gamma}\Big) \tag{32}$$

So, the relation is:

$$\Delta\bar{x}_i = \Delta\bar{x}_0 - \Delta\bar{x}_0 \frac{i}{N-1}\Big(1 - \frac{1}{\gamma}\Big) \tag{33}$$

However, taking into account that γ and N are specified parameters, the goal is to obtain a relation between $\Delta\bar{x}_0$ and $\Delta\bar{x}_e$. A key point here is that, even though the spacing between edges has changed, the length of the block hasn't. Thus:

$$\bar{L} = \sum_{i=0}^{N-1} \Delta\bar{x}_e = \sum_{i=0}^{N-1} \Delta\bar{x}_i \tag{34}$$

If the right hand side of the equation is expanded:

$$\bar{L} = \sum_{i=0}^{N-1} \Delta\bar{x}_0 - \Delta\bar{x}_0 \frac{i}{N-1}\Big(1 - \frac{1}{\gamma}\Big) \tag{35}$$

Separating the two terms:

$$\bar{L} = \sum_{i=0}^{N-1} \Delta\bar{x}_0 - \sum_{i=0}^{N-1} \Delta\bar{x}_0 \frac{i}{N}\Big(1 - \frac{1}{\gamma}\Big) \tag{36}$$

The first sum is well known:

$$\sum_{i=0}^{N-1} \Delta\bar{x}_0 = \Delta\bar{x}_0 \sum_{i=0}^{N-1} 1 = \Delta\bar{x}_0 N \tag{37}$$

On the other hand, the second sum results in:

$$\sum_{i=0}^{N-1} \Delta\bar{x}_0 \frac{i}{N-1}\Big(1 - \frac{1}{\gamma}\Big) = \frac{\Delta\bar{x}_0}{N-1}\Big(1 - \frac{1}{\gamma}\Big) \sum_{i=0}^{N-1} i = \frac{\Delta\bar{x}_0}{N-1}\Big(1 - \frac{1}{\gamma}\Big)\Big(\frac{N(N-1)}{2}\Big) \tag{38}$$

Inserting the results (37) and (38) in equation (36):

$$\bar{L} = \Delta\bar{x}_0 N - \Delta\bar{x}_0\Big(1 - \frac{1}{\gamma}\Big)\Big(\frac{N}{2}\Big) \tag{39}$$

It can be checked from this result that, if there is no gradient ($\gamma = 1$), $\Delta\bar{x}_0 = \Delta\bar{x}_e$. Thus, at the end of the calculation, a relation between the length of the block in the $\bar{x}$ direction ($\bar{L}$) and the distance between the first two edges with gradient γ ($\Delta\bar{x}_0$) appears. This allows to calculate the distance between the last two edges $\Delta\bar{x}_{N-1}$ and, therefore, to maintain the continuity of the spacing between edges when joining the regions $\bar{x} < -\Pi_l/2$ with $\bar{x} \in [-\Pi_l/2, \Pi_l/2]$ and $\bar{x} > \Pi_l/2$. Considering the distance between the last two edges (condition 3), the relation is:

$$\Delta\bar{x}_{N-1} = 2\frac{\bar{L}}{N}\Big(\gamma + \frac{1}{\gamma}\Big)^{-1} \tag{40}$$

As can be seen in figure 12, where a a mesh composed of 3 blocks, such as the finite crack one (see section 4.4.3), is presented, the distribution of edges is regular, that is, it does not present abrupt jumps between blocks, as it is intended with this meshing strategy.

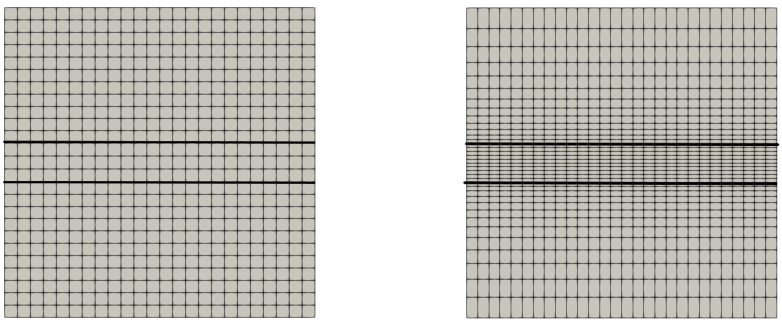

(a) (b)

Figure 12: (a) Three block mesh without gradient and (b) same mesh with $\gamma \neq 1$ calculated by (40).

4.5.2 Mesh refinement

Another method to increase the mesh resolution in some regions in OpenFoam is to divide the hexahedrons that are in the region of interest. Unlike the gradient method, mesh refinement increases the computational resources because the number of nodes increases. The implementation of the refinements in OpenFoam consists of:

1. Selecting the nodes of the mesh that are within the region of interest. With this objective, geometrical entities (spheres, cylinders, boxes,...) are defined in the mesh inside which the selected nodes remain.
2. Once the nodes of the region of interest are selected, these are divided until the desired spatial resolution is achieved.

As mentioned before, the interest of implementing mesh refinements is that there are regions that are physically more interesting, since they are the ones in which the variables change more rapidly. In particular, during the multiple simulations that have been carried out in this work, several special interest zones have been identified: the crack and the laser spot. In order to mesh these regions with enough spatial resolution, a region proportional to the non-dimensional thermal diffusion length has been carefully refined.

With the objective of refining the region close to the crack, the box geometry has been used as it keeps the aspect ratio with the sample. Furthermore, during the simulations that have been carried out, it has been noticed that a single box refinement not only increases significantly the resolution in that region but also reduces both the number of nodes far from the crack and consequently, the computational time. An example of this refinement can be found in figure 13 (a).

In addition to the meshing of the crack or the region close to it, an important aspect in IR thermography simulations is to correctly mesh the region in which the laser is introduced. In order to complete this task, the cylinder refinement has been chosen as it keeps the aspect ratio with the circular geometry of the laser spot. During the multiple simulations done in this work, it has been tested that refining the cells of the laser environment three times, each time with cylinders of smaller height and radius, it is enough to capture the laser spot appropriately. This triple refinement can be seen in figure 13 (b). When both of these refinements are combined (see figure 13 (c)), as it is the case of this work, the resulting mesh ends up having on the order of 250000 nodes.

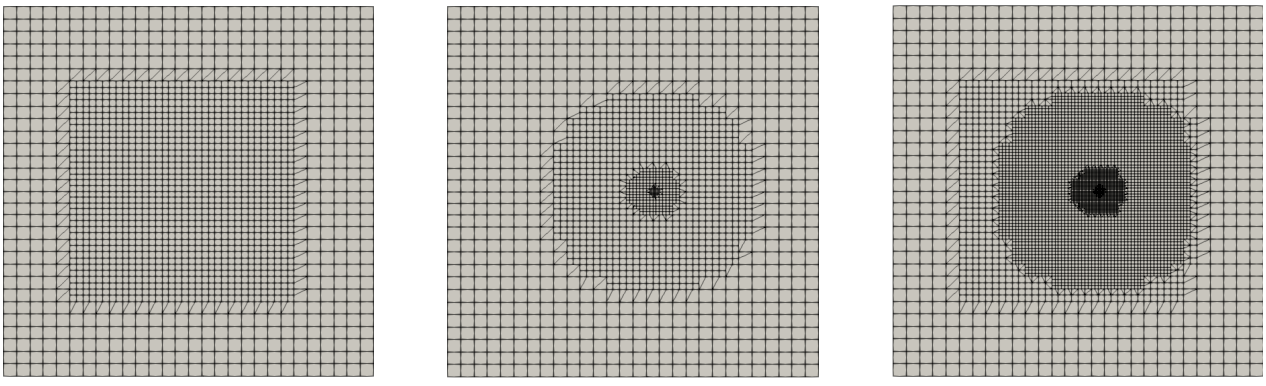

(a) (b) (c)

Figure 13: (a) Single box, (b) triple cylinder refinements and (c) both of them combined.

4.6 Processing

Once the mesh is done, the equations must be solved. At this stage of the calculation, known as processing, it is worth to notice that even though only the stationary part of the problem is being simulated, for numerical reasons, it may happen that the first oscillations do not represent that part correctly until a few iterations are done. Therefore, in order to find the stable stationary situation without undesired numerical effects a criterion that guarantees the appropriate stationary nature of the calculation is required. In this work this criterion has been selected as the full reproducibility of the obtained thermal waves.

Programmatically, the implementation of this condition has been carried out selecting an arbitrary point of the stationary thermal cycle and checking its value over cycling, provided an appropriate time resolution. When the temperature difference between cycles, i.e., the slope of the line joining two consecutive points (as can be seen in figure 14) is found to be below an imposed threshold value, the criterion is satisfied and the next cycle is saved as the stationary oscillation for each node of the mesh.

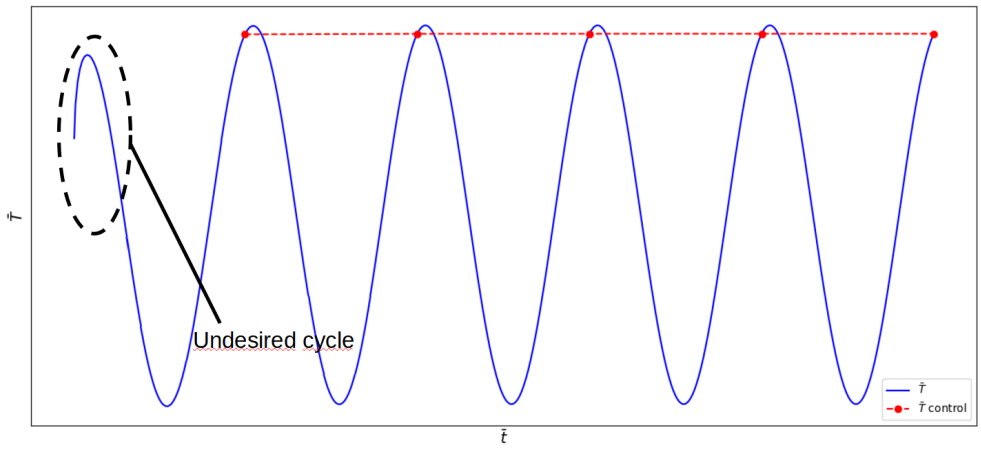

Figure 14: Temperature evaluation of an arbitrary point over cycling until the stationary stability criterion is satisfied.

4.7 Post-Processing

As mentioned before, one of the consequences of treating this problem in a simple way, from the mathematical point of view, is that instead of solving the Helmoltz equation [4] which integrates the harmonic nature of the lock-in experiment, the heat equation is solved. Whereas the first provides direct solution for the thermal amplitude, the second doesn't, resulting the temperature field. The consequence of this is that, after the processing stage, those amplitudes must be found. This is the post-processing stage of the calculation.

In this stage, even if the temperature field for the complete sample is calculated, the results presented in this work are limited to a line perpendicular to the crack and crossing the center of the laser spot. This selection has been done as this would be the physically more significant region. Once the region to plot the non-dimensional temperature amplitudes is chosen, the maximum and minimum values of each thermal wave are programmatically searched, leading to the non-dimensional temperature amplitude plot.

5 Results

5.1 Validation of the model

Once the dimensionless numerical model has been established, its validity must be checked. Although the model can be validated against experimental data, in this case it is going to be done against analytical or numerical models, depending on the situation. In this section first, the comparisons of the results of the dimensionless model with the analytical model corresponding to a vertical infinite crack [1] will be presented in figure 15. Second, the non-dimensional results for semi-infinite and finite cracks are going to be validated against another numerical model developed by R.Celorrio et al. [4] (in the following, DG FEM model) written in FEniCS, due to the fact that there is no analytical solution in these cases. The associated results in this case are shown in figures 16 and 17. In order to make the cases as realistic as possible, it has been decided to validate the model with typical experimental parameter values (see table 4) and for two materials: AISI 304 and Cu (see their thermal properties in table 1).

P (W)	r_g (mm)	f (Hz)	(x_0, y_0) (mm)
1	0.165	1	(0,0.5)

Table 4: Dimensional parameter values that have been used in order to validate the dimensionless numerical model.

Aiming to compare the results between models, the dimensional results are transformed to dimensionless following the scale variables previously introduced (see equation (13)). In order to maintain an acceptable sensitivity of the temperature changes, even far from the heat source, instead of the amplitude its natural logarithm is plotted. The dimensionless parameters that have been used can be found in table 5.

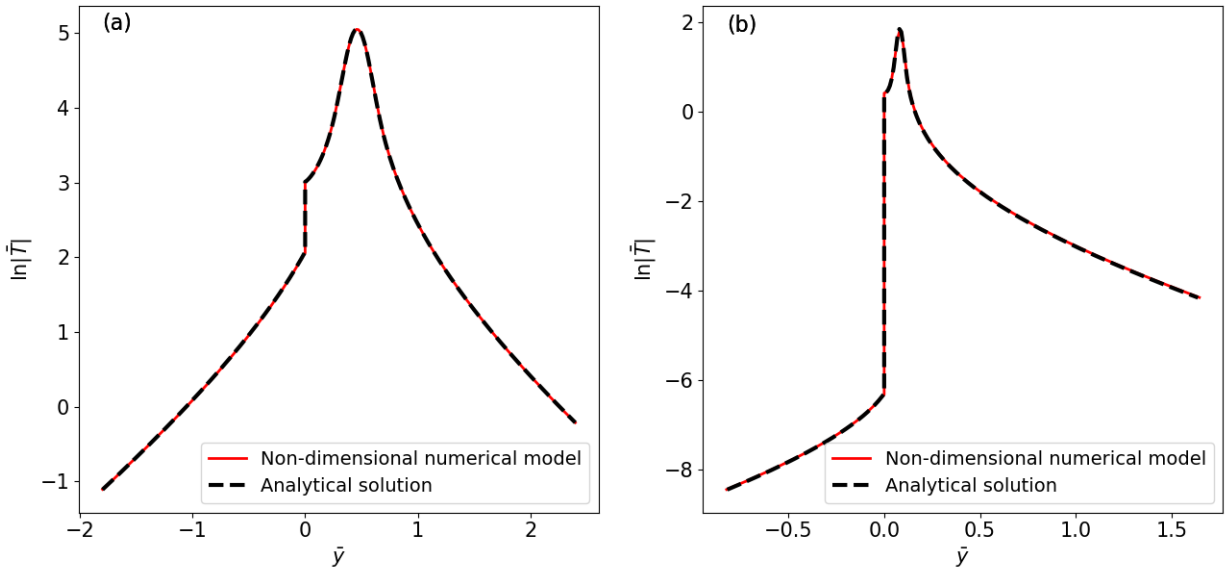

Figure 15: Comparison between the non dimensional numerical results and analytical solution for infinite vertical cracks. (a) AISI 304 and (b) Cu.

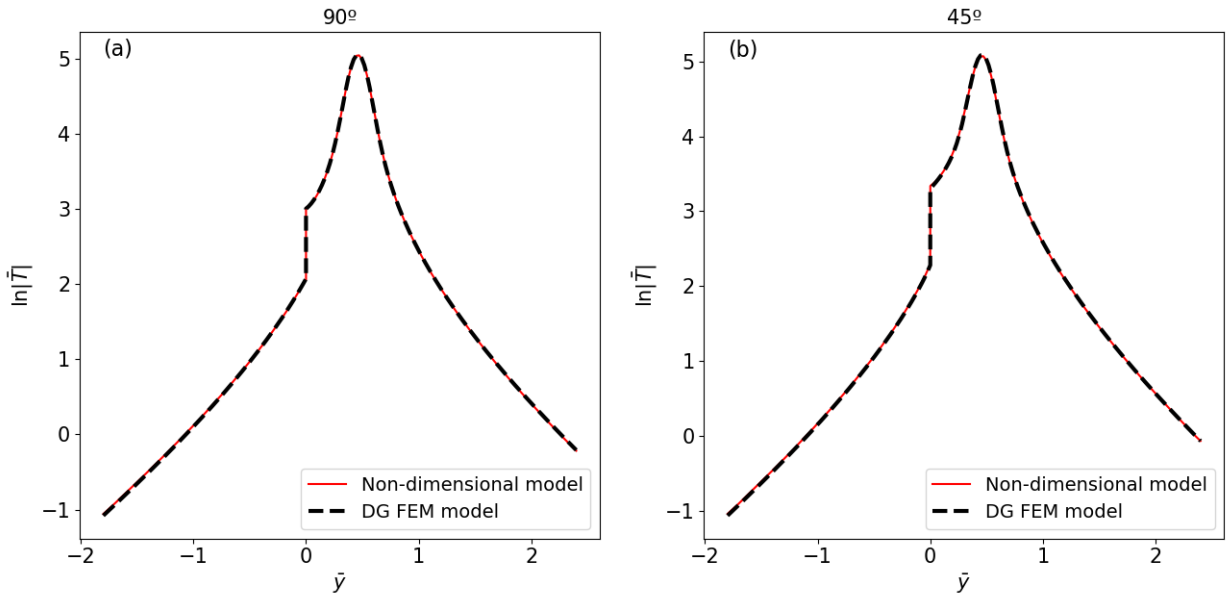

Figure 16: Comparison between the non dimensional results and the DG FEM model in the semi-infinite crack case in AISI 304 for two different crack inclinations. (a) 90º and (b) 45º.

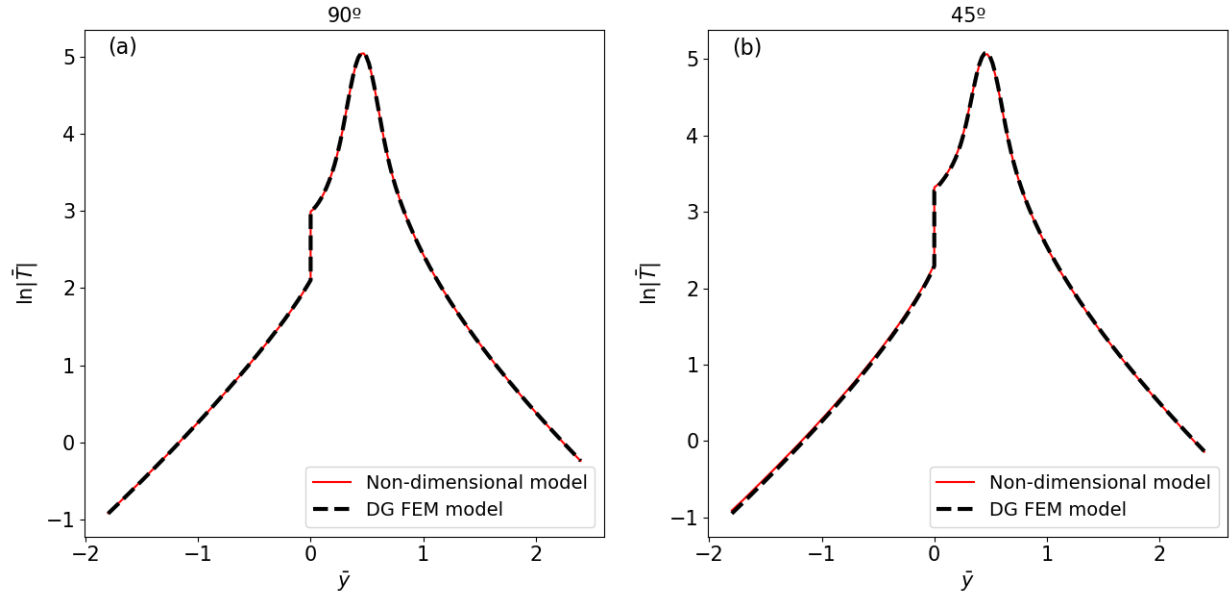

Figure 17: Comparison between the non dimensional results and the DG FEM model in the finite crack case in AISI 304 for two different crack inclinations. (a) 90º and (b) 45º.

In order to quantify the differences between the dimensional (analytical or numerical) and dimensionless models, among all the statistical options, in this work the root mean square error (RMSE) has been chosen due to the ease of interpreting the results. As it can be seen in figures 15, 16 and 17 the agreement between all the models is very satisfactory in the three presented cases, the values presented in table 6, are going to be discussed in detail in section 6.1.

	Figure 15 (a)	Figure 15 (b)	Figure 16	Figure 17
Type of crack	Infinite	Infinite	Semi-Infinite	Finite
$\mathbf{\Pi_1}$	23528	4191	23528	23528
$\mathbf{\Pi_2}$	0.023	0.0007	0.023	0.023
$\mathbf{\Pi_3}$	586	15899	586	586
$\mathbf{\Pi}_w$	0.00092	0.0082	0.00092	0.00092
$\mathbf{\Pi}_l$	-	-	-	0.92
$\mathbf{\Pi}_d$	-	-	0.92	0.92
$\bar{y}_0$	0.46	0.45	0.46	0.46
$\boldsymbol{\theta}$(º)	90	90	90/45	90/45

Table 5: Dimensionless parameters used to obtain the results shown in figures 15, 16 and 17.

Case / Model	Analytical	DG FEM model
Infinite 90º (I) (figure 15 (a))	0.017	-
Infinite 90º (II) (figure 15 (b))	0.014	-
Semi-infinite 90º (figure 16 (a))	-	0.009
Semi-infinite 45º (figure 16 (b))	-	0.012
Finite 90º (figure 17 (a))	-	0.0027
Finite 45º (figure 17 (b))	-	0.022

Table 6: RMSE of the comparisons shown in figures 15, 16 and 17.

5.2 Parametric analysis

In this section a catalog of curves in which each non-dimensional parameter is varied, while the others are fixed, is shown. This catalog has two main purposes. First, it can be used as a result guideline for a variety of experimental and material properties parameters. Going more in detail, the second purpose of this catalog, is to provide a parametric analysis showing the influence of each non-dimensional parameter in the resulting thermal amplitude ($|\bar{T}|$) plot.

Although it is a common practice to normalize the experimental data in order to eliminate the effect of parameters which are difficult to control, such as the absorption coefficient (η) in equation (11), the normalization can also limit the amount of information obtained in the experiment. In order to take advantage of both methodologies, in this work, as general rule, both normalized and non-normalized plots are shown[2].

All of the results presented in this section are obtained for a finite crack, as it is the most versatile one. The experimental parameters that lead to these simulations are typical values of experimental setups. It is worth to notice that the power of this non-dimensional formulation lies in the fact that the result is not dependent on each individual experimental parameter, but depends only on their combinations. The dimensionless parameters that remain fixed in each calculation are specified in table 7.

[2]In the results in which the normalization does not have any impact, only the normalized natural logarithm of the thermal amplitude $ln(|\bar{T}_n|)$ is shown.

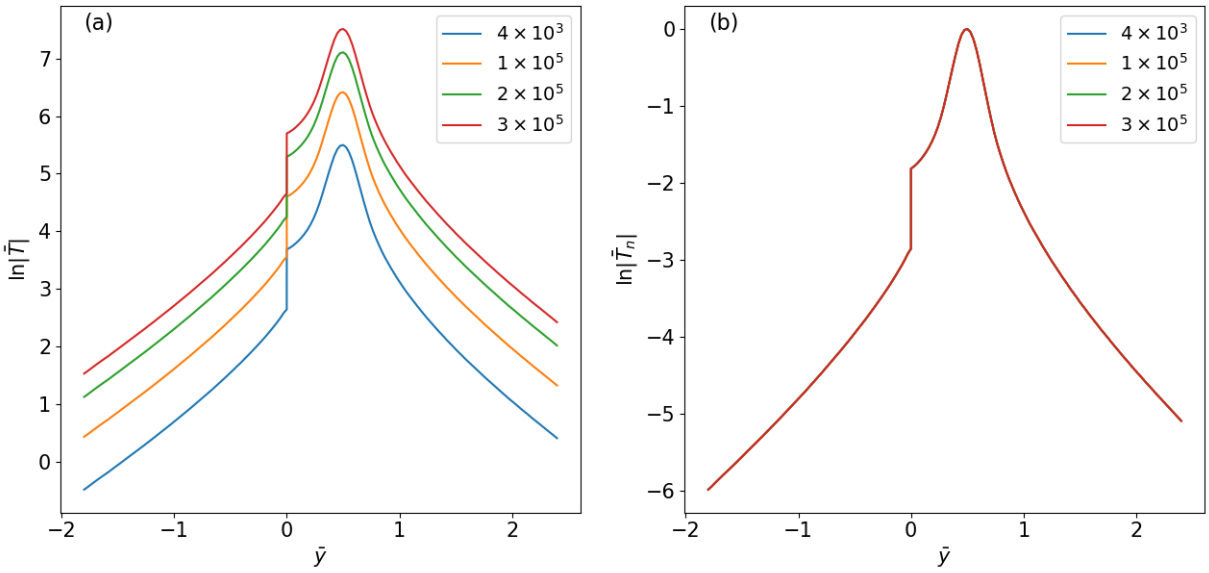

Figure 18: Natural logarithm plot of the thermal amplitude (a) non-normalized and (b) normalized on the transverse sample profile for $\Pi_1 = 4 \times 10^3, 1 \times 10^5, 2 \times 10^5, 3 \times 10^5$.

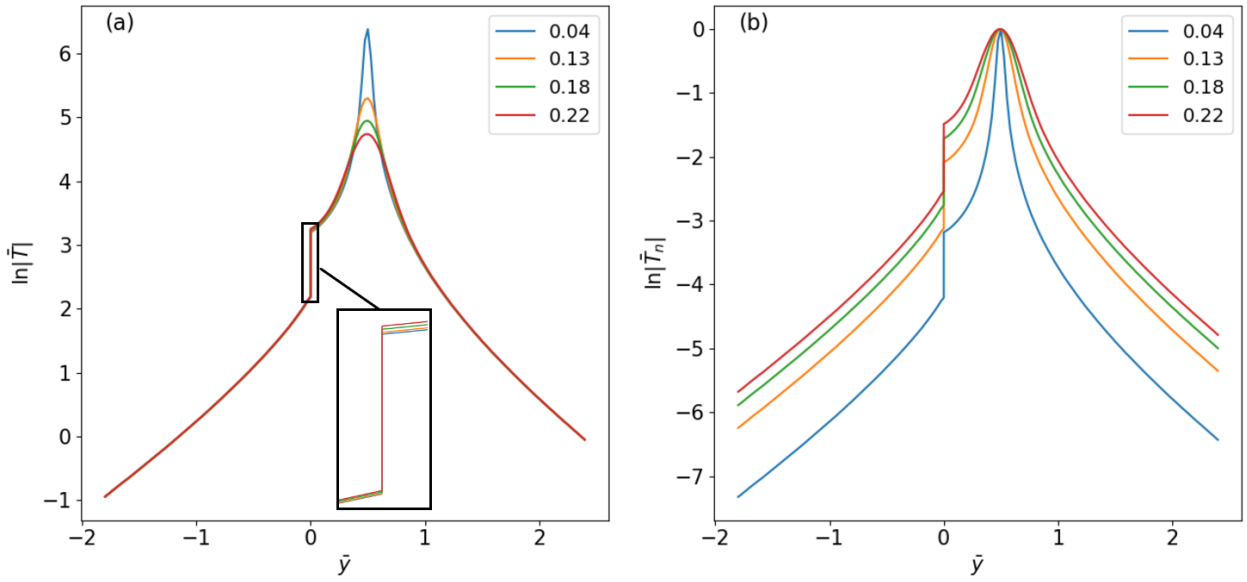

Figure 19: Natural logarithm plot of the thermal amplitude (a) non-normalized, showing the zoomed amplitude jump associated to the crack in the insert and (b) normalized on the transverse sample profile for $\Pi_2 = 1 \times 10^{-7}, 2 \times 10^{-7}, 3 \times 10^{-7}, 1 \times 10^{-8}$.

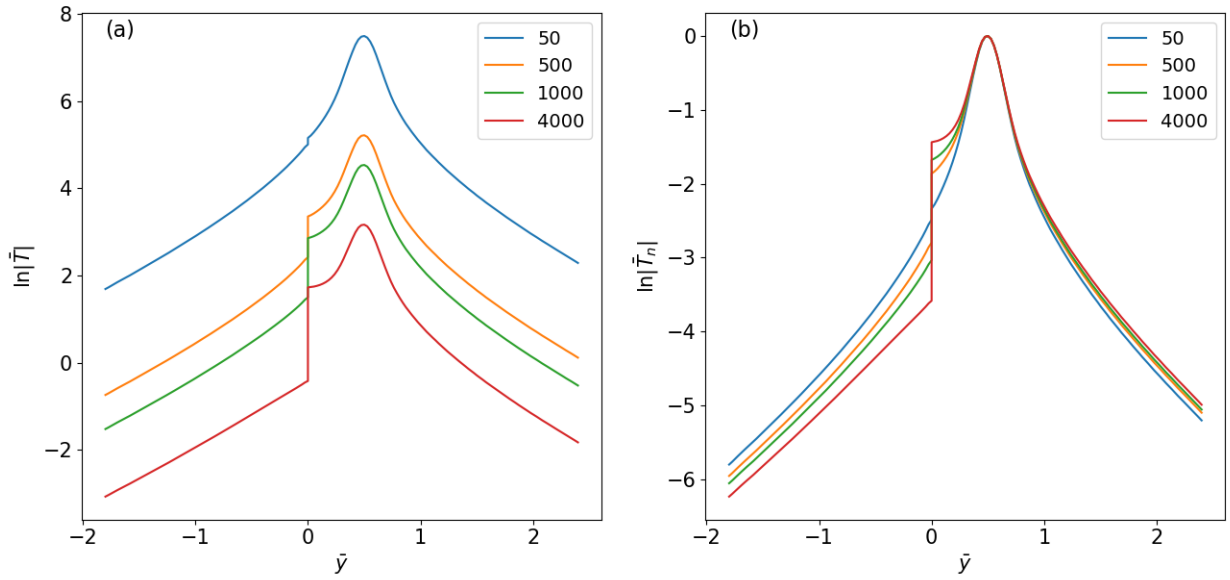

Figure 20: Natural logarithm plot of the thermal amplitude (a) non-normalized and (b) normalized on the transverse sample profile for $\Pi_3 = 50, 500, 1000, 4000$.

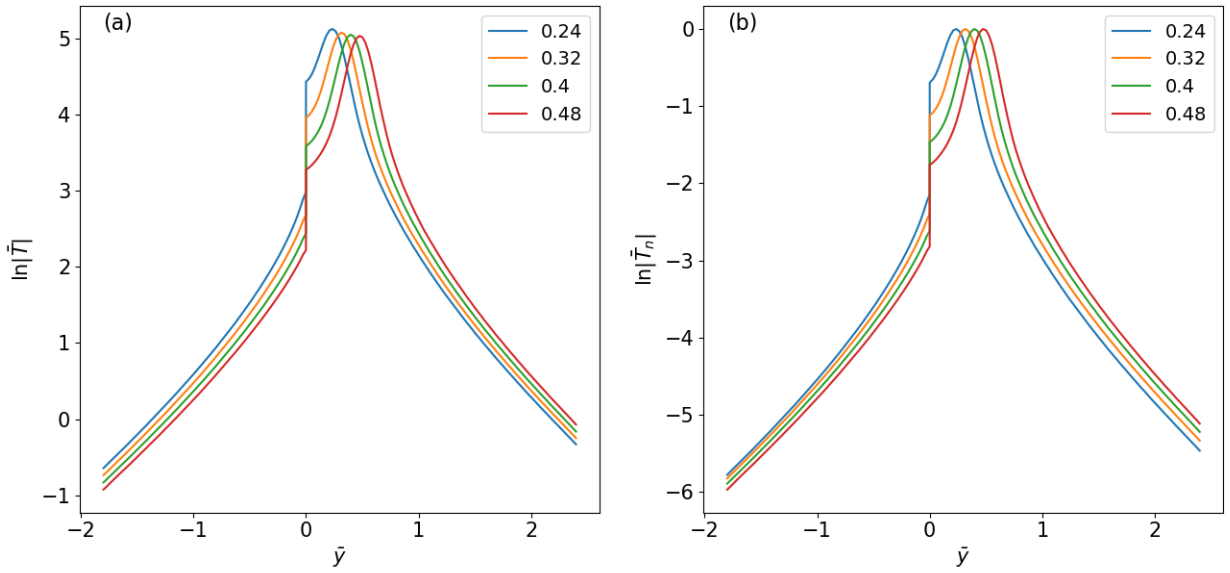

Figure 21: Natural logarithm plot of the thermal amplitude (a) non-normalized and (b) normalized on the transverse sample profile for $\bar{y}_0 = 0.24, 0.32, 0.40, 0.48$.

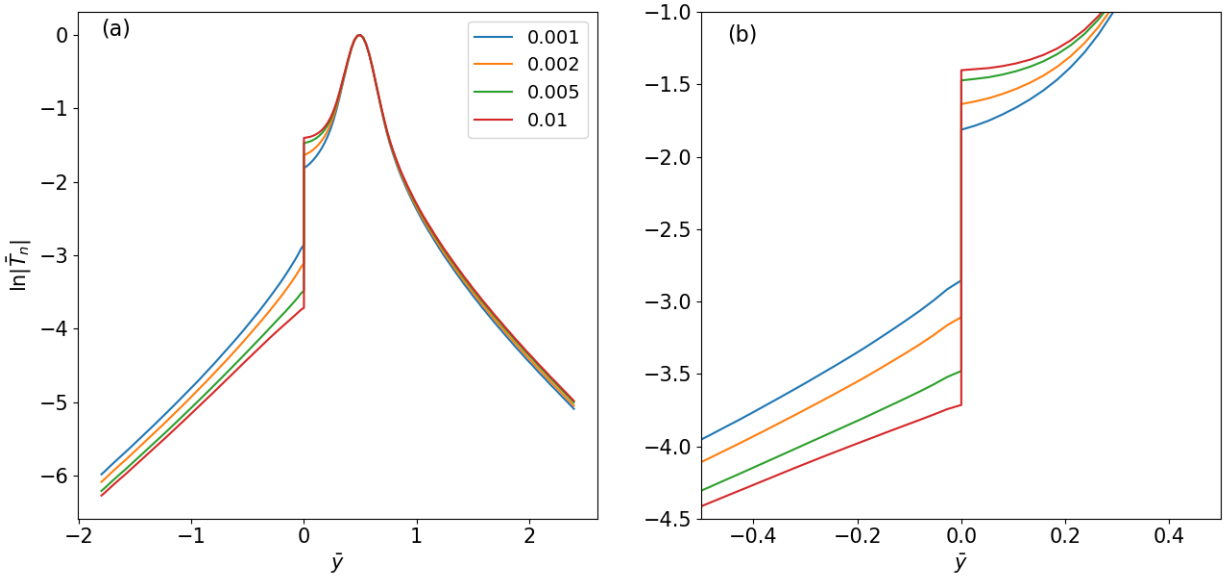

Figure 22: Natural logarithm plot of the thermal amplitude (a) normalized and (b) crack region zoomed on the transverse sample profile for $\Pi_w = 0.001, 0.002, 0.005, 0.01$.

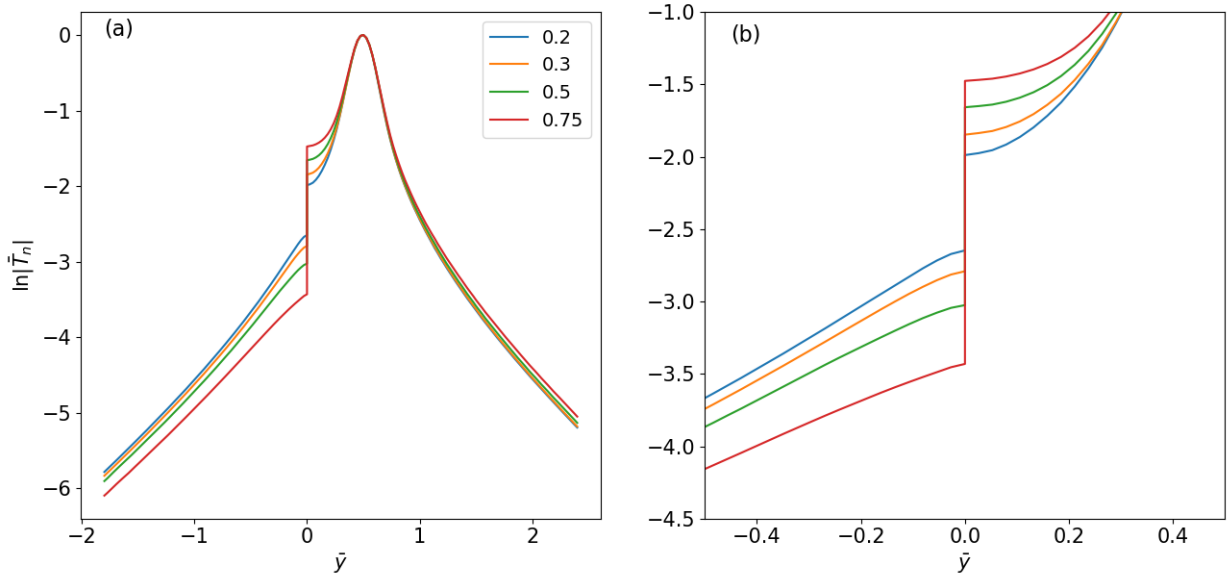

Figure 23: Natural logarithm plot of the thermal amplitude (a) normalized and (b) crack region zoomed on the transverse sample profile for $\Pi_l = 0.2, 0.4, 0.5, 0.75$.

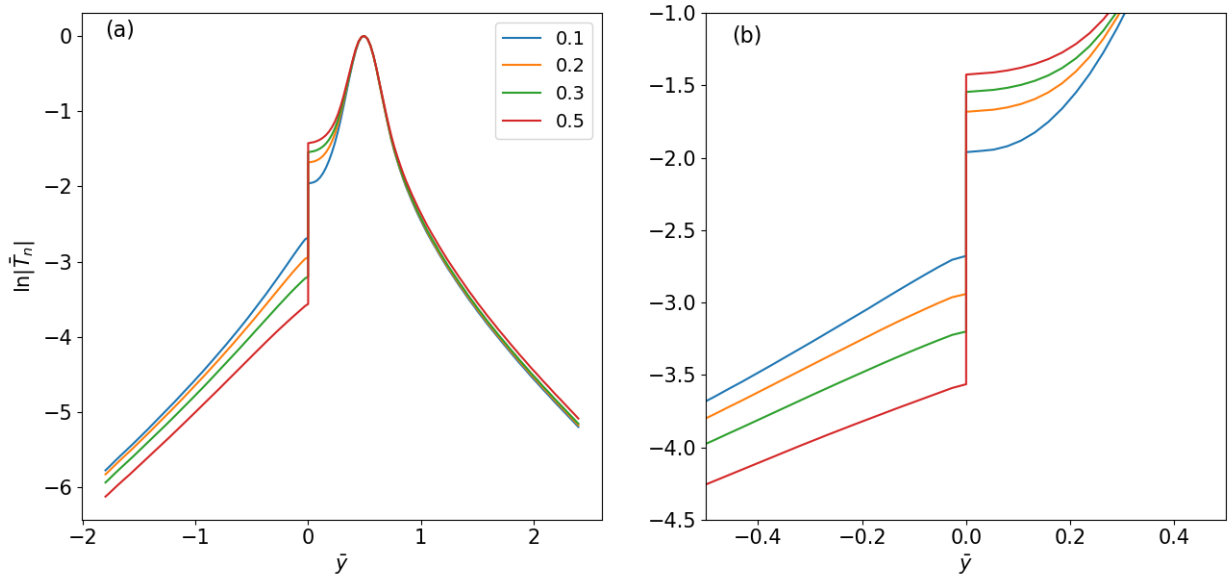

Figure 24: Natural logarithm plot of the thermal amplitude (a) normalized and (b) crack region zoomed on the transverse sample profile for $\Pi_d = 0.1, 0.2, 0.3, 0.5$.

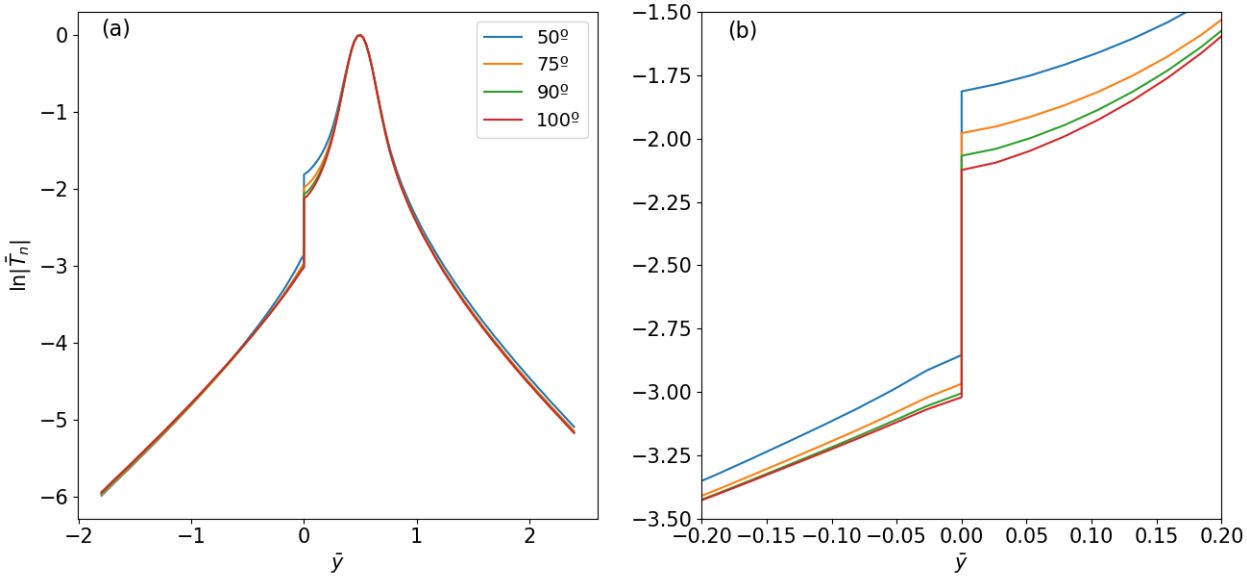

Figure 25: Natural logarithm plot of the thermal amplitude (a) normalized and (b) crack region zoomed on the transverse sample profile for $\theta = 50º, 75º, 90º, 100º$.

Figure	$\mathbf{\Pi_1}$	$\mathbf{\Pi_2}$	$\mathbf{\Pi_3}$	$\bar{y}_0$	$\mathbf{\Pi}_w$	$\mathbf{\Pi}_l$	$\mathbf{\Pi}_d$	$\boldsymbol{\theta}$ (º)
18	-	0.027	600	0.50	0.001	1	1	50
19	25231	-	600	0.50	0.001	1	1	50
20	25231	0.027	-	0.50	0.001	1	1	50
21	25231	0.027	600	-	0.001	1	1	50
22	25231	0.027	600	0.50	-	1	1	50
23	25231	0.027	600	0.50	0.001	-	1	50
24	25231	0.027	600	0.50	0.001	1	-	50
25	25231	0.027	600	0.50	0.001	1	1	-

Table 7: Parameters used to obtain each figure of the catalog.

6 Discussion

6.1 Validation of the model

As mentioned before, in order to quantify the differences between models, the RMSE has been chosen. However, by itself this value is not representative since its magnitude is highly dependant on the scale on which the natural logarithm of the thermal amplitudes ranges. It is worth to notice that, typically, for the performed calculations, the difference between the maximum and the minimum of $ln|\bar{T}|$ is, in absolute value, about 6. This means that, for example, a RMSE ≥ 0.5 (relative error approximately greater than 10%) can be considered as a bad result while RMSE ≤ 0.1 (relative error approximately lower than 2%) can be considered good enough.

The comparison with the analytical model is shown in figure 15. It can be seen that, qualitatively, the results obtained with both models present a high level of agreement. Quantitatively, after a very detailed study of the two results, a small difference in the amplitude jump is observed. In the analytical model this jump is purely vertical, since the crack leads to a temperature discontinuity. On the other hand, in the non-dimensional model continuous finite elements are used, which means that the temperature is a continuous function projected in all the spatial domain. Hence, a vertical discontinuity with this formulation is completely impossible. However, the obtained results lead to 0.34% and 0.14% relative errors respectively, which shows that the results agree correctly and reaffirms the fact that the difference between models appears only in practically imperceptible details.

To strengthen the validity of the dimensionless model, it is also necessary to compare results with other types of cracks. As previously mentioned, there is no analytical solution for vertical non-infinite cracks, so the comparison has been done with another numerical model [4]. The results of this comparison are shown in figures 16 and 17. In table 6 it can be seen that, the obtained RMSE in the semi-infinite (0.009 and 0.012 for the 90º and 45º cases respectively) and for the 90º finite case (0.0027), are small values taking into account that the results range from $ln|\bar{T}| \approx -1$ to $ln|\bar{T}| \approx 5$, that is, the obtained relative errors are 0.15%, 0.2% and 0.045% respectively. This small differences are due to the fact that the dimensional model used for comparison deploys discontinuous FEM (which allows to achieve a jump completely vertical) while, for the same reason that has been explained for the validation with the analytical model, with the dimensionless formulation presented in this work it is not possible to achieve purely vertical thermal amplitude jumps.

In the case of finite cracks inclined 45º, 17 (b), a small difference is observed in the $\bar{y} < 0$ region far from the heat source. This difference is due to the meshing strategy that has been followed. In this work, the mesh has been made with the aim of achieving a high resolution in a very close region to the crack without having to spend much computational resources doing each simulation. This means that the density of nodes is lower far from the crack ($|\bar{y}| > 1$). Therefore, a little bit of resolution is lost in that region and it leads to small differences between models. Since the spatial dimensions in this model are scaled by the thermal diffusion length, this loss of resolution appears at regions close to the limit to which the heat will reach, so, they can be acceptable provided that the obtained RMSE demonstrates that there is a high agreement between the two results.

Overall, the obtained RMSE results show a relative error of around 0.4% of the range of $ln|\bar{T}|$ at most, which is an extremely low percentage. In this line, consequently, the comparisons provide a very good agreement which confirms that the model performs correctly.

6.2 Parametric analysis

Once the non-dimensional model has been validated against the analytical and another numerical model, the effect of varying each dimensionless parameter can be studied.

6.2.1 Π_1

The effect of varying Π_1 is shown in figure 18. In figure 18 (a) can be seen that increasing Π_1 results in shifting the thermal amplitude upwards. It is worth to notice that, even though this parameter is the combination of the power of the laser, μ, T_0 and the air conductivity, its effect is to increase the overall temperature amplitude. However, as it can be seen in figure 18 (b), once the thermal amplitude is normalized, no change is observed due to variation of Π_1. As a consequence the variation of this parameter leads to a pure vertical translation with no influence in the morphology of the amplitude curve.

6.2.2 Π_2

When the second parameter, Π_2, is varied the resulting thermal amplitude plot changes in two main aspects. The first thing that can be seen in figure 19 (a) is that when Π_2 decreases the maximum value of the natural logarithm thermal amplitude increases. However, when the results are normalized (see 19 (b)), the full width at half maximum (FWHM) is also reduced. The reason is that, even though this parameter is the Gaussian radius divided by the thermal diffusion length, it is essentially the one that controls the Gaussian radius of the laser. This means that if the laser is focused in a smaller region (lower Π_2), its FWHM will also be smaller. However, since it is the same laser, its energy must be the same regardless of Π_2. As the energy is related with the area under the curve, this leads to a greater maximum. This change in the FWHM, which is unique among all dimensionless parameters, makes each thermal amplitude plot with different value of Π_2 unique.

The second effect of changing Π_2 can be seen in the insert of figure 19 (a). Here it can be noticed that the value of the discontinuity is slightly greater for increasing values of Π_2. This can be physically interpreted taking into account the relation between this parameter and r_g. In this line, this tiny difference appears because when the non-dimensional radius of the laser is larger, it is in some sense closer to the crack, which leads to slightly higher temperatures on that side.

6.2.3 Π_3

Changing Π_3 shares with the change in Π_1 and Π_2 the effect of shifting the natural logarithm of the thermal amplitude. In this case, what it is seen is that when Π_3 decreases the $ln|\bar{T}|$ plot shifts upwards and vice versa. However, as Π_3 is somehow a dimensionless thermal conductivity, its change results in two more significant changes in the results.

The first one is in the value of the discontinuity. As the value of Π_3 is increased, the temperature jump due to the crack is greater. This effect can be seen in figure 20 and can be understood as a serial association of the material of thermal conductivity Π_3 and the crack of conductivity $(\Pi_3)_{air} = 1$. If Π_3 is a large number, then the equivalent thermal resistance of the system will be practically that of the air and, therefore, there will be lower temperatures in the other side of the crack. On the other hand, if

Π_3 is a small number, both non-dimensional thermal conductivities will be similar and, consequently, the drop in temperature will be less significant.

Another aspect that distinguishes two thermal amplitude plots, with different values of Π_3, is their slope far from the heat source. As it can be seen in figure 20 (b), the smaller is Π_3, the more pronounced the slope will be. Returning to the physical interpretation that has been given to this parameter previously, this result is what one would expect. If the non-dimensional thermal conductivity is small, then the thermal amplitude far from the heat source will be also small, in other words, the temperature will practically not change with respect to the initial. Therefore the thermal amplitude will fall faster, that is, the absolute value of the slope will increase.

6.2.4 $\bar{y}_0$

When the dimensionless position of the laser ($\bar{y}_0$) is varied, three significant changes appear in the results. The first difference is the most obvious one: a horizontal displacement for increasing values of $\bar{y}_0$. Interpreting $\bar{y}_0$ as the non-dimensional position of the laser, this was an expected result because, when the energy is placed for larger values of $\bar{y}_0$, the maximum is shifted in that direction. However, no other dimensionless parameter causes this effect, meaning that each thermal amplitude plot is, as it happens for Π_2, completely unique.

The second one is the value of the jump of the thermal amplitude. As it can be seen in figure 21 (b), the lower is the $\bar{y}_0$ value, the higher the jump is. Mathematically, this results makes full sense because the jump is proportional to $\bar{\nabla}\bar{T}$, and this term is larger when the value of this parameter is smaller. Physically this can be interpreted taking into account the relation between $\bar{y}_0$ and the position of the laser. In this line, bringing the laser closer to the crack means that the thermal amplitude on that side will be higher and, therefore, the jump will be higher as well.

The third change, that can be clearly seen in figure 21 (a), is a different maximum value of $ln|\bar{T}|$ for decreasing values of $\bar{y}_0$. The reason may be the reflexion of the thermal wave travelling backwards from the crack which leads to a net temperature amplitude increasing effect not appreciable if the laser is 'far' enough from the crack. However, a more precise analysis would be needed to clarify this effect.

6.2.5 Π_w, Π_l, Π_d and θ

If the geometry of the crack is changed the resulting thermal amplitude plots (figures 22, 23 and 24) present an double change: the amplitude jump on the discontinuity and the slopes far from the heat source. When the non-dimensional width (Π_w), length (Π_l) or depth (Π_d) decreases, the obtained results show that the value of the jump also decreases. In this line, this is a coherent result due to the fact that in the limit of null values for Π_w, Π_l, Π_d there wouldn't be any discontinuity and hence, no jump either.

In those figures it can be seen that not only the jump of thermal amplitude changes but also the slopes far from the heat source. In fact, this effect is much more pronounced in the non-illuminated side of the crack ($\bar{y} < 0$) than in the illuminated side. All in all, it is worth to notice that the effect of these three parameters is quite similar, which means that, far from making the results unique, a quasi-degeneracy is obtained.

On the contrary, the effect of reducing the angle θ leads to higher thermal amplitude jumps. As can be seen in figure 25 (b), not only the jump of temperature is larger but it starts at higher temperatures when the angle of inclination decreases, which may be due to an 'accumulation' of heat in the illuminated side of the crack. However, this hypothesis must be studied in detail in future work.

6.2.6 Non-dimensional parameter combinations

Once the effect of each individual dimensionless parameter has been discussed, the analysis can be extended discussing the effect of combinations of them. It must be noted that the understanding of the potential degeneracy of this thermographic problem becomes of paramount importance when the identification of experimental or material properties is desired based on the experimental results (inverse problem).

Taking into account the previously derived dimensionless mathematical formulation of the described phenomena (see equation (27)), it is not hard to see that if:

$$\frac{\Pi_1}{\Pi_3} = \frac{(\Pi_1)'}{(\Pi_3)'} \quad \text{and} \quad \Pi_3\Pi_w = (\Pi_3)'(\Pi_w)' \tag{41}$$

the equations don't change, and consequently the result doesn't change either. In order to confirm this statement, in figure 26 two calculations, carried out with two different (Π_1, Π_3, Π_w) triples satisfying the condition (41) can be seen.

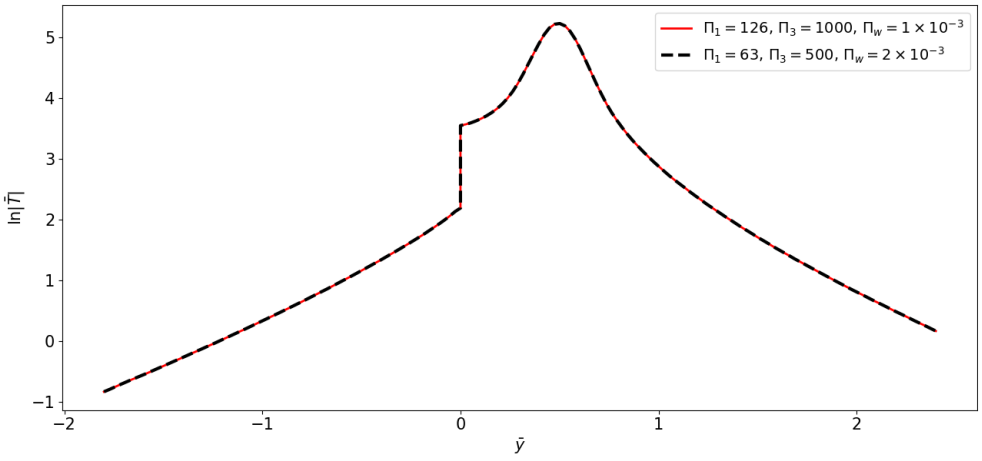

Figure 26: Natural logarithm plot of the thermal amplitude on the transverse sample profile for two different (Π_1, Π_3, Π_w) triples which satisfy (41).

Therefore, the results of validating this condition lead to go beyond the formulation of what has previously been shown and combine this three parameters as follows. Starting with the laser spot boundary condition (24) and multiplying and dividing it by Π_w:

$$\left.\frac{\partial \bar{T}}{\partial \bar{z}}\right|_{\bar{z}=0} = \frac{\Pi_1\Pi_w}{\Pi_2\Pi_3\Pi_w} e^{-\frac{2}{\Pi_2}\left[(\bar{x}-\bar{x}_0)^2+(\bar{y}-\bar{y}_0)^2\right]} \cos(2\bar{t}) \tag{42}$$

Introducing the following new variables:

$$\chi_1 \equiv \Pi_1\Pi_w, \quad \chi_2 \equiv \Pi_2, \quad \chi_3 \equiv \Pi_3\Pi_w \tag{43}$$

where the variable χ_2 has been introduced in order to maintain the same notation for all the parameters, this boundary condition becomes:

$$\frac{\partial \bar{T}}{\partial \bar{z}}\Big|_{\bar{z}=0} = \frac{\chi_1}{\chi_2\chi_3} e^{-\frac{2}{\chi_2}\left[(\bar{x}-\bar{x}_0)^2+(\bar{y}-\bar{y}_0)^2\right]} \cos(2\bar{t}) \tag{44}$$

On the other hand, after introducing these new variables, the temperature jump condition associated with the crack (26) becomes:

$$\Delta\bar{T} = \chi_3 \bar{\nabla}\bar{T} \quad \text{if} \quad \bar{x} \in \Big[-\frac{\chi_l}{2}, \frac{\chi_l}{2}\Big], \quad \bar{z} \in \Big[0, \chi_d\Big] \tag{45}$$

being $\chi_l \equiv \Pi_l$ and $\chi_d \equiv \Pi_d$. Summarizing, the previously derived non-dimensional formulation (27), can be reformulated as follows:

$$\boxed{\begin{cases} \bar{\nabla}^2\bar{T} = \frac{\partial \bar{T}}{\partial \bar{t}} \\ \frac{\partial \bar{T}}{\partial \bar{z}}\Big|_{\bar{z}=0} = \frac{\chi_1}{\chi_2\chi_3} e^{-\frac{2}{\chi_2}\left[(\bar{x}-\bar{x}_0)^2+(\bar{y}-\bar{y}_0)^2\right]} \cos(2\bar{t}) \\ [[\dot{\bar{Q}}]] = 0 \\ \Delta\bar{T} = \chi_3 \bar{\nabla}\bar{T} \end{cases}} \tag{46}$$

This set of equations reformulates the problem that has been studied in this work, removing the degeneracy found in Π_1/Π_3 and $\Pi_3\Pi_w$. It is worth to notice that, by the definition of χ_1:

$$\chi_1 \equiv \Pi_1\Pi_w = \frac{2Pwf}{\alpha T_0 \kappa_{air}} \tag{47}$$

And the definition of χ_3:

$$\chi_3 \equiv \Pi_3\Pi_w = \frac{\kappa}{\kappa_{air}} \frac{w}{\sqrt{\frac{\alpha}{\pi f}}} \tag{48}$$

any combination of the experimental and material parameters that lead to the same values of χ_1 and χ_3 will result in the same thermal amplitude plot.

However, in the parametric analysis it has been mentioned that the effect of the first dimensionless parameter Π_1 on the thermal amplitude plot is to shift the results upwards or downwards. As a consequence, if the temperature amplitude is normalized, the results are unaffected by Π_1. This leads to conclude that the previously introduced condition (41) can be reduced, if the thermal amplitude is normalized, to:

$$\Pi_3\Pi_w = (\Pi_3)'(\Pi_w)' \tag{49}$$

Figure 27 shows two calculations carried out with two different combinations of Π_3 and Π_w that satisfy condition (49). This results confirm the degeneracy of the system in relation with χ_3 parameter.

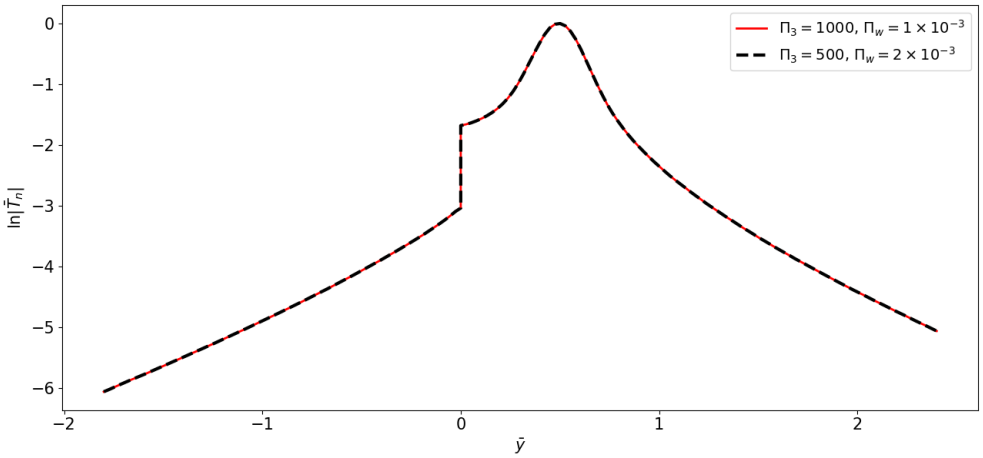

Figure 27: Natural logarithm plot of the thermal amplitude on the transverse sample profile for two different (Π_3, Π_w) tuples which satisfy (49).

Overall, the identification of these combinations of parameters of show the power of the non-dimensional formulation of the problem.

7 Conclusions

In this work a non-dimensional FEM model for crack characterization in aerospace materials by means of lock-in IR thermography has been developed. In addition to the resolution of the equations, the optimization of the spatial domain to be modeled has been carried out through different meshing strategies, such as non-regular edge distribution or selective refinements of the mesh. These meshing strategies have optimized the calculations in terms of accuracy and computational resources.

The developed model shows a very good agreement when compared with other analytical or numerical models, although the formulation of each one has a slight impact on the results. Overall, the comparisons show very low relative errors (at most 0.4%) which confirm the remarkable accuracy of the developed model.

The dimensionless model has allowed a general interpretation of the lock-in IR thermography experiment not depending on the parameters of the material or the experimental ones, but on the dimensionless parameters identified. These parameters have been used to perform a parametric analysis where their effect in the thermal amplitude plots has been analyzed.

While the effect of Π_1 is removable by normalization, the effect of Π_3 cannot be isolated in just one zone of the curve since it affects the morphology of the entire thermal amplitude plot. On the other hand, despite of different morphological reshaping of the curve, the effect of Π_2 and $\bar{y}_0$ has turned out to be unique, i.e., it is impossible to obtain the same thermal amplitude plot with different values of these. It has been seen that, although the most prominent effect of Π_w, Π_l, Π_d and θ is to change the amplitude jump, they also show other secondary effects in other regions such as the slopes far from the heat source. Moreover, except for θ, in the other three parameters those secondary effects can be seen more clearly on the non-illuminated side of the crack.

Even though it is beyond the scope of this work, the results obtained for the parametric analysis carried out allow to determine where the sensitivity of the curves is to each of the parameters. This becomes of paramount importance when parametric inversion is performed.

Going further in the developed non-dimensional discussion, the degeneracy of the thermographic problem has been addressed. In this line, a non-dimensional reformulation of the problem has been presented. It has been demonstrated that there is no need to distinguish between Π_1, Π_3 and Π_w, since different combinations of these parameters lead to the same results. This work has allowed to determine which combinations of experimental parameters and material properties leading to the same amplitude thermograms which are hardly accessible by other procedures.

As a potential continuation of the developed investigation the following future work is identified:

1. The study of the degeneracy of the non-dimensional formulation searching other potential parametric combinations.
2. The development of inverse models which make use of the non-dimensional formulation presented in this work.
3. The introduction of more general crack geometries beyond planar.

References

[1] N. Pech-May, A. Oleaga, A. Mendioroz, A. Omella, R. Celorrio, and A. Salazar, "Vertical cracks characterization using lock-in thermography: I infinite cracks," *Measurement Science and Technology*, vol. 25, no. 11, p. 115601, 2014.

[2] R. Celorrio, A. Omella, N. Pech-May, A. Oleaga, A. Mendioroz, and A. Salazar, "Vertical cracks characterization using lock-in thermography: Ii finite cracks," *Measurement Science and Technology*, vol. 25, no. 11, p. 115602, 2014.

[3] S. Findlay and N. Harrison, "Why aircraft fail," *Materials Today*, vol. 5, pp. 18–25, 11 2002.

[4] R. Celorrio, A. Omella, A. Mendioroz, A. Oleaga, and A. Salazar, "Advances in crack characterization by lock-in infrared thermography," *International Journal of Thermophysics*, vol. 36, no. 5, pp. 1202–1207, 2015.

[5] S. Sfarra, E. Marcucci, D. Ambrosini, and D. Paoletti, "Infrared exploration of the architectural heritage: from passive infrared thermography to hybrid infrared thermography (hirt) approach," *Materiales de Construcción*, vol. 66, no. 323, pp. e094–e094, 2016.

[6] J. Rodríguez-Aseguinolaza, M. Colom, J. González, A. Mendioroz, and A. Salazar, "Quantifying the width and angle of inclined cracks using laser-spot lock-in thermography," *NDT & E International*, vol. 122, p. 102494, 2021.

[7] D. P. Almond and S. Lau, "Defect sizing by transient thermography. i. an analytical treatment," *Journal of Physics D: Applied Physics*, vol. 27, no. 5, p. 1063, 1994.

[8] J. G. Sun, "Analysis of Pulsed Thermography Methods for Defect Depth Prediction," *Journal of Heat Transfer*, vol. 128, no. 4, pp. 329–338, 10 2005. [Online]. Available: https://doi.org/10.1115/1.2165211

[9] J. Laskar, S. Bagavathiappan, M. Sardar, T. Jayakumar, J. Philip, and B. Raj, "Measurement of thermal diffusivity of solids using infrared thermography," *Materials Letters*, vol. 62, no. 17-18, pp. 2740–2742, 2008.

[10] A. A. Badghaish and D. C. Fleming, "Non-destructive inspection of composites using step heating thermography," *Journal of composite materials*, vol. 42, no. 13, pp. 1337–1357, 2008.

[11] M. Colom, J. Rodriguez-Aseguinolaza, A. Mendioroz, and A. Salazar, "Imaging real cracks: evaluation of the depth and width of narrow fatigue cracks in and al-alloys using laser-spot lock-in thermography," in *Thermosense: Thermal Infrared Applications XLIII*, vol. 11743. International Society for Optics and Photonics, 2021, p. 117430F.

[12] G. Nikishkov, "Introduction to the finite element method," *University of Aizu*, pp. 1–70, 2004.

[13] Á. J. O. Milián, "Resolución numérica de problemas inversos en termografía activa para la caracterización de grietas," Ph.D. dissertation, Universidad de Zaragoza, 2017.

[14] H. P. Langtangen and G. K. Pedersen, "Basic partial differential equation models," in *Scaling of Differential Equations*. Springer, 2016, pp. 69–98.

[15] Thermtest instruments, "Materials Thermal Properties Database," https://thermtest.com/thermal-resources/materials-database, Accessed: 9/5/2022.

[16] OpenFoam, "OpenFoam," www.openfoam.org, Accessed: 11/6/2022.

[17] H. G. Weller, G. Tabor, H. Jasak, and C. Fureby, "A tensorial approach to computational continuum mechanics using object-oriented techniques," *Computers in physics*, vol. 12, no. 6, pp. 620–631, 1998.

[18] H. Jasak, A. Jemcov, Z. Tukovic *et al.*, "Openfoam: A c++ library for complex physics simulations," in *International workshop on coupled methods in numerical dynamics*, vol. 1000. IUC Dubrovnik Croatia, 2007, pp. 1–20.

[19] M. Colom, A. Bedoya, A. Mendioroz, and A. Salazar, "Measuring the in-plane thermal diffusivity of moving samples using laser spot lock-in thermography," *International Journal of Thermal Sciences*, vol. 151, p. 106277, 2020.

[20] N. J. Wallace, N. B. Crane, and M. R. Jones, "Defect measurement limits using flash thermography with application to additive manufacturing," *NDT & E International*, vol. 128, p. 102615, 2022.

[21] M. Krishnapillai, R. Jones, I. H. Marshall, M. Bannister, and N. Rajic, "Ndte using pulse thermography: Numerical modeling of composite subsurface defects," *Composite Structures*, vol. 75, no. 1-4, pp. 241–249, 2006.

[22] R. Biswas and R. C. Strawn, "Tetrahedral and hexahedral mesh adaptation for cfd problems," *Applied Numerical Mathematics*, vol. 26, no. 1-2, pp. 135–151, 1998.